








ARTICLE

# iASPP contributes to cell cortex rigidity, mitotic cell rounding, and spindle positioning

Aurélie Mangon<sup>1</sup> , Danièle Salaün<sup>1</sup>, Mohamed Lala Bouali<sup>1</sup> , Mira Kuzmić<sup>1</sup>, Sabine Quitard<sup>1</sup>, Sylvie Thuault<sup>1</sup> , Daniel Isnardon<sup>1</sup>, Stéphane Audebert<sup>1</sup> , Pierre-Henri Puech<sup>2</sup> , Pascal Verdier-Pinard<sup>1</sup> , and Ali Badache<sup>1</sup> 

**iASPP is a protein mostly known as an inhibitor of p53 pro-apoptotic activity and a predicted regulatory subunit of the PP1 phosphatase, which is often overexpressed in tumors. We report that iASPP associates with the microtubule plus-end binding protein EB1, a central regulator of microtubule dynamics, via an SxIP motif. iASPP silencing or mutation of the SxIP motif led to defective microtubule capture at the cortex of mitotic cells, leading to abnormal positioning of the mitotic spindle. These effects were recapitulated by the knockdown of the membrane-to-cortex linker Myosin-Ic (Myo1c), which we identified as a novel partner of iASPP. Moreover, iASPP or Myo1c knockdown cells failed to round up upon mitosis because of defective cortical stiffness. We propose that by increasing cortical rigidity, iASPP helps cancer cells maintain a spherical geometry suitable for proper mitotic spindle positioning and chromosome partitioning.**

## Introduction

In symmetric cell division, placement of the mitotic spindle at the cell center and orientation along the future axis of cell division is a prerequisite for equal distribution of the cellular material to the daughter cells (Kiyomitsu, 2015). Spindle positioning is driven by pulling forces exerted on astral microtubules by the cortically anchored minus-end-directed motor complex dynein-dynactin (Du et al., 2001; di Pietro et al., 2016). Anchoring of the motor proteins involves a well-conserved ternary complex, including  $\alpha$ -subunits of heterotrimeric G proteins, LGN (Leu-Gly-Asp repeat protein), and the nuclear and mitotic apparatus protein (NuMA), which interacts with the dynein-dynactin complex and microtubules (Lu and Johnston, 2013; Du et al., 2001). Appropriate positioning of the mitotic spindle during cell division also depends on cell morphogenetic reorganization. Indeed, epithelial cells undergo dramatic changes in shape and mechanics as they progress through cell division. Mitotic entry is associated with focal adhesions disassembly; osmotic swelling, which results in increased cell tension; and rearrangement of the cortical actomyosin network, leading to increased cortex rigidity. Altogether, this enables cells to adopt a close-to-spherical shape, providing a suitable environment for spindle assembly and accurate partitioning of chromosomes into the daughter cells (Ramkumar and Baum, 2016). Cortex stiffening requires uniform activation of myosin-II-mediated

cortical contractility downstream of the RhoA exchange factor Ect2, but also requires tight membrane-to-cortex attachment. In *Drosophila melanogaster* cells, this is likely to be mediated by the ezrin-radixin-moesin (ERM) family of proteins (Carreno et al., 2008; Kunda et al., 2008). In mammalian cells, the molecular mechanism is less clear, as ERMs do not appear to be required for cell rounding (Machicoane et al., 2014). Class 1 myosins, monomeric molecular motors that bind actin filaments via their motor domain and membranes via their tail domain, are possible candidates as they were shown to cross-link the plasma membrane to the cortex in brush border cells, skin fibroblasts, and primary macrophages (Nambiar et al., 2009; Venit et al., 2016; Barger et al., 2019). However, their role during mitotic rounding was not explored.

Mitotic rounding is of particular importance for cells dividing in confined environments. In packed epithelia, mitotic rounding defects lead to abnormal spindle orientation and asymmetric division (Chanet et al., 2017; Luxenburg et al., 2011). Cells growing in three-dimensional confining devices preventing rounding display spindle assembly defects and delayed mitotic progression (Lancaster et al., 2013). Cancer cells must be able to divide in a wide range of environments: in the primary tumors, in the circulating system, and at metastatic sites. Recent evidence shows that oncogenic signals promote cortical rigidity to facilitate division of cancer cells in mechanically confined

<sup>1</sup>Centre de Recherche en Cancérologie de Marseille, Institut National de la Santé et de la Recherche Médicale, Institut Paoli-Calmettes, Aix-Marseille Université, Centre National de la Recherche Scientifique, Marseille, France; <sup>2</sup>Laboratoire Adhésion et Inflammation, Institut National de la Santé et de la Recherche Médicale, Centre National de la Recherche Scientifique, Aix Marseille Université, Turing Center for Living Systems, Marseille, France.

Correspondence to Ali Badache: [ali.badache@inserm.fr](mailto:ali.badache@inserm.fr); Pascal Verdier-Pinard: [pascal.verdier-pinard@inserm.fr](mailto:pascal.verdier-pinard@inserm.fr).

© 2021 Mangon et al. This article is distributed under the terms of an Attribution-Noncommercial-Share Alike-No Mirror Sites license for the first six months after the publication date (see <http://www.rupress.org/terms/>). After six months it is available under a Creative Commons License (Attribution-Noncommercial-Share Alike 4.0 International license, as described at <https://creativecommons.org/licenses/by-nc-sa/4.0/>).

environments (Matthews et al., 2020; Hosseini et al., 2020), in accordance with the hypothesis that regulators of the actomyosin cortex can be coopted by cancer cells to successfully divide in environments with diverse physical properties (Matthews and Baum, 2012). The mechanisms underlying the stiffening of the cell cortex in mitosis is still incompletely known. A systematic search for cues mediating increased rounding force and pressure of mitotic cell uncovered dozens of potential candidates (Toyoda et al., 2017), including many regulators of the actin cytoskeleton, but few regulators of the mitotic spindle or astral microtubules.

Microtubule function is modulated by microtubule-associated proteins, including plus-end tracking proteins (+TIPs), a large and diverse family of proteins that share the ability to bind growing microtubule plus-ends. EB1 is a hub in the complex network of +TIPs. It directly interacts with microtubule plus-ends and recruits many other proteins harboring SxIP or CAP-Gly motifs to control microtubule dynamics and mediate their association with the cell cortex (Akhmanova and Steinmetz, 2008). The systematic investigations of the EB1 protein-protein interaction has revealed numerous potential EB1 partners (Bouguenina et al., 2017; Jiang et al., 2012) that might differentially contribute to regulate microtubule properties or mediate crosstalk with the cellular cortex.

Here, we investigated the unexplored connection between EB1 and inhibitor of ASPP (iASPP) and its impact on mitotic spindle positioning and astral microtubule crosstalk with the cell cortex. iASPP is a member of the ASPP (apoptosis-stimulating protein of p53) family of proteins (Bergamaschi et al., 2003), which share the ability to interact with the p53 tumor suppressor via their C-terminal SH3 domain to modulate the expression of pro-apoptotic target genes. iASPP also interacts with PP1 and could function as a PP1 regulatory subunit (Zhou et al., 2019; Skene-Arnold et al., 2013). iASPP is overexpressed in many types of tumors and contributes to tumor progression and resistance to treatment (Bergamaschi et al., 2003; Lu et al., 2013; Jiang et al., 2011; Morris et al., 2014; Zhang et al., 2005; Ge et al., 2017). We identify and validate a specific motif that mediates iASPP binding to EB1. We show that iASPP knockdown or disruption of iASPP-EB1 interaction leads to abnormal centering of the mitotic spindle, associated with asymmetric astral microtubule capture, and defective rounding of mitotic cells. This is recapitulated by the knockdown of the class 1 myosin Myo1c (myosin-Ic), which we identify as a novel partner of iASPP. iASPP or Myo1c knockdown results in a significant decrease of cortex rigidity, which is restored by ectopic expression of cortex-membrane cross-linkers. Altogether, we propose that iASPP and Myo1c are important for mitotic cell cortex stiffening, cell rounding, and correct positioning of the spindle, which is required for the appropriate distribution of genetic material to daughter cells.

## Results

### iASPP interacts with PP1 and EB1

We had previously performed a systematic investigation of the protein interaction network of EB1 in SKBr3 cells stably

expressing EB1-GFP and identified several potential EB1 partners, including iASPP (Bouguenina et al., 2017). We first confirmed that iASPP is an actual partner of EB1. iASPP coprecipitated with ectopically expressed EB1 in three different cell lines (Fig. 1 A). Ectopically expressed EB1 fused to the promiscuous biotin ligase BirA (Roux et al., 2012) biotinylated iASPP in situ, verifying that iASPP-EB1 interaction occurred in intact cells (Fig. 1 B). We also tagged endogenous EB1 via CRISPR/Cas9-mediated knock-in of GFP11 (corresponding to the 11th  $\beta$ -strand of the GFP  $\beta$ -barrel structure) in a HeLa cell line expressing the complementary GFP1-10 fragment. Coexpression of EB1-GFP11, under the control of the endogenous promoter, and GFP1-10 allows the reconstitution of a functional GFP tag (Leonetti et al., 2016). We verified that EB1 expressed under the control of the endogenous promoter coprecipitated endogenous iASPP (Fig. 1 C and Fig. S1 A). EB1-binding proteins, when overexpressed, form comets at microtubule plus-ends, regardless of their actual subcellular localization at endogenous levels. Overexpressed GFP-tagged iASPP colocalized with EB1 at microtubule plus-ends and formed typical comets (Fig. 1 D).

iASPP antibodies did not allow us to verify the coprecipitation of endogenous iASPP and EB1. This might be due to the poor affinity of the antibodies and/or the low levels of expression of iASPP. We thus tagged endogenous iASPP with multiple copies of GFP11 via CRISPR/Cas9-mediated gene editing of HeLa<sup>GFP1-10</sup> cells. Using this cell line, which expressed iASPP associated with (multiple) reconstituted GFP proteins, we could confirm that iASPP expressed under the control of its endogenous promoter interacted with endogenous PP1 and EB1 (Fig. S1, B and C).

We evaluated the ability of iASPP constructs with mutations of specific motifs or domains (Fig. 1 E) to interact with EB1 and PP1 (Fig. 1 F). WT iASPP interacted robustly with PP1. The interaction was lost when the <sup>622</sup>RARL<sup>625</sup> PP1-binding motif (Skene-Arnold et al., 2013) was mutated to RARA or when the SH3 domain was deleted. iASPP C-terminal folded region (Cter; 600-828) was sufficient for the robust association of PP1 via the cooperative contribution of the RARL motif, the Ank repeats, and the SH3 domain (Fig. S1 D).

In transient transfections, iASPP interaction with EB1 was generally below detection levels (Fig. 1 F) unless we also overexpressed tagged EB1 (Fig. 1 G), indicating that EB1 had a weaker affinity for iASPP than PP1. Mutation of iASPP <sup>350</sup>SRIP<sup>353</sup> motif to SRNN prevented both coimmunoprecipitation of EB1 (Fig. 1 G) and colocalization with EB1 at microtubule plus-ends (Fig. 1 D). Interestingly, EB1 binding was stronger for iASPP constructs defective for PP1 binding (iASPP-RARA and iASPP- $\Delta$ SH3) and was maximal for iASPP- $\Delta$ Ank-SH3, which lacks the entire folded region (Fig. 1, F and G), indicating that PP1 and the C-terminal region hinder iASPP-EB1 interaction. Proximity biotinylation, using iASPP constructs fused to BirA, confirmed that the same pattern of interactions occurred in situ (Fig. 1 H). Of note, we have not been able to detect the interaction of iASPP with p53 in the cellular models used here, neither by coimmunoprecipitation nor by proximity biotinylation.

It was suggested that iASPP constitutes homodimers in the cytoplasm via head-to-tail N-terminal to C-terminal binding (Lu et al., 2013). We confirmed that the iASPP N-terminal region

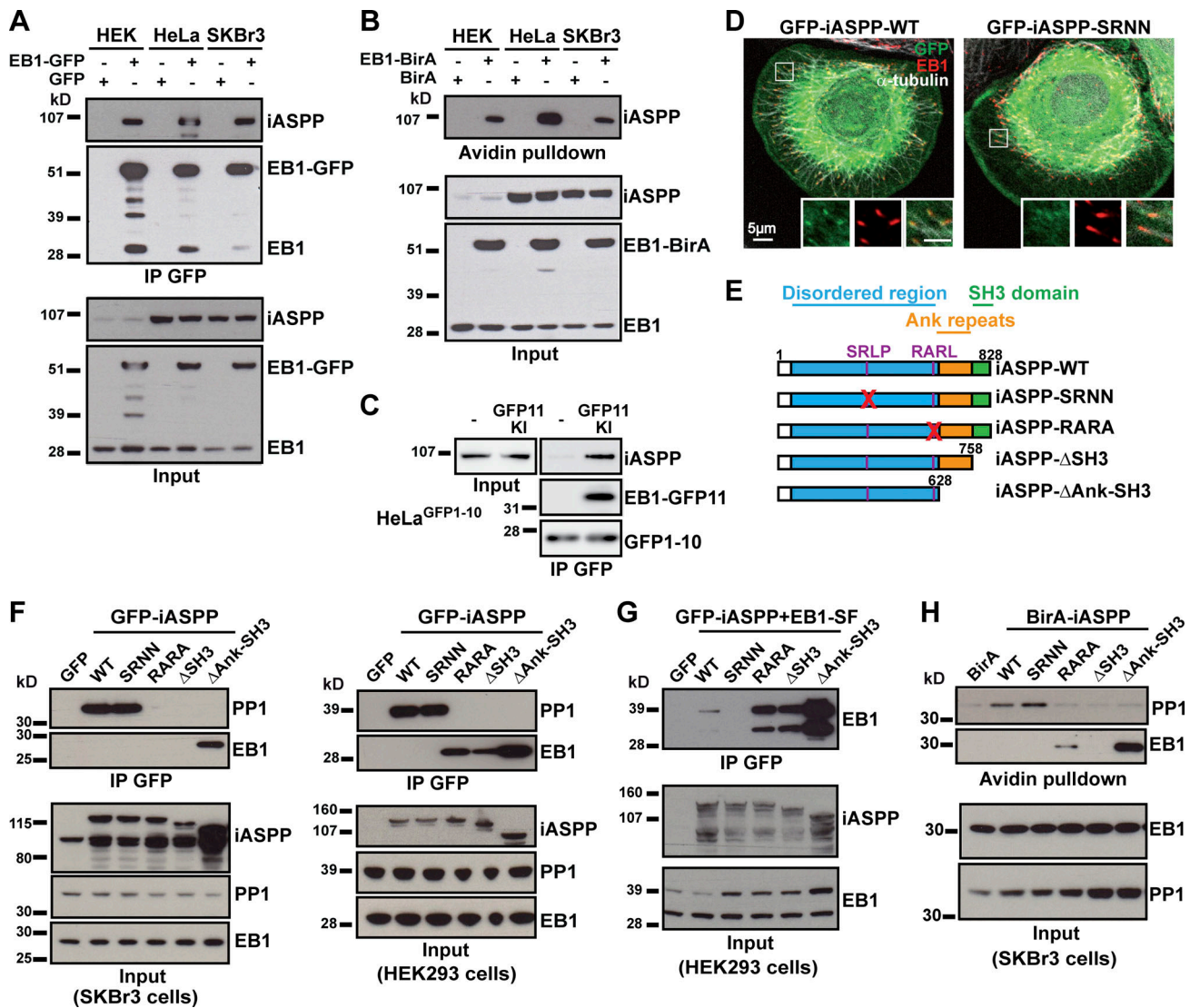


Figure 1. **iASPP associates with EB1.** (A) EB1-GFP or GFP was expressed in the indicated cell lines before immunoprecipitation (IP) with GFP-Trap and WB analysis. (B) EB1-BirA or BirA was expressed in the indicated cell lines before addition of biotin, isolation of the biotinylated proteins with avidin-coated beads, and WB analysis. (C) Endogenous EB1 tagged with GFP interacts with endogenous iASPP. EB1 was C-terminally tagged via knock-in (KI) of GFP11 in HeLa<sup>GFP1-10</sup> cells. EB1-GFP was pulled down via GFP-Trap and iASPP coprecipitation analyzed by WB. (D) Co-localization of iASPP, but not iASPP-SRNN, with EB1 at microtubule plus-ends was determined by immunolabeling of EB1 and microtubules in SKBr3 cells expressing GFP-iASPP or GFP-iASPP-SRNN. Inserts: zoomed images of the boxed regions; scale bar is 10 μm. (E) Representations of iASPP constructs used in the study. iASPP displays a predicted disordered region (blue) that includes a putative SxIP motif and a noncanonical PP1-binding motif. Ank repeats and SH3 folded domains are indicated. Red Xs designate the position of the mutated amino acid residue. (F–H) Identification of motifs and domains required for EB1 and PP1 binding. GFP-iASPP, BirA-iASPP, and SF-EB1 constructs were expressed in cells before IP (F and G) or biotinylation (H) and analysis of coprecipitated/biotinylated PP1 and EB1 by WB.

(1–290) interacted with the C-terminal region whether we pulled down the C-terminal fragments (Fig. 2 A) or the N-terminal fragments (Fig. 2 B). The interaction was actually much stronger with longer fragments (1–599 or 1–628) corresponding to the entire disordered region (Fig. 2, A–C), with the (290–382) sequence showing the strongest contribution (Fig. 2, D and E). On the C-terminal side, the combined contribution of the ankyrin repeats and the SH3 domain was required (Fig. 2 F). Interestingly, PP1 binding to the C-terminal region considerably prevented N-terminal binding (Fig. 2, A–C). To confirm the ability of iASPP to homodimerize, we coexpressed two different iASPP constructs, one with a GFP tag and the other with a

Strep-Flag (SF) tag in HEK293 cells. Surprisingly, pulling down one construct did not coprecipitate the other construct (Fig. 2 G). In a parallel experiment, EB1-GFP robustly coprecipitated with EB1-SF (Fig. 2 G), as expected for a protein that functions as a dimer (Sen et al., 2013). Inefficient dimerization was not due to steric hindrance by the bulky GFP tag, as constructs with small tags positioned on the C- or N-terminal extremities of iASPP were likewise unable to dimerize (Fig. S1 E); PP1, on the other hand, was efficiently coprecipitated with all iASPP constructs (Fig. S1 E). Thus, iASPP supramolecular organization does not involve homodimerization, but rather association with PP1 and EB1.



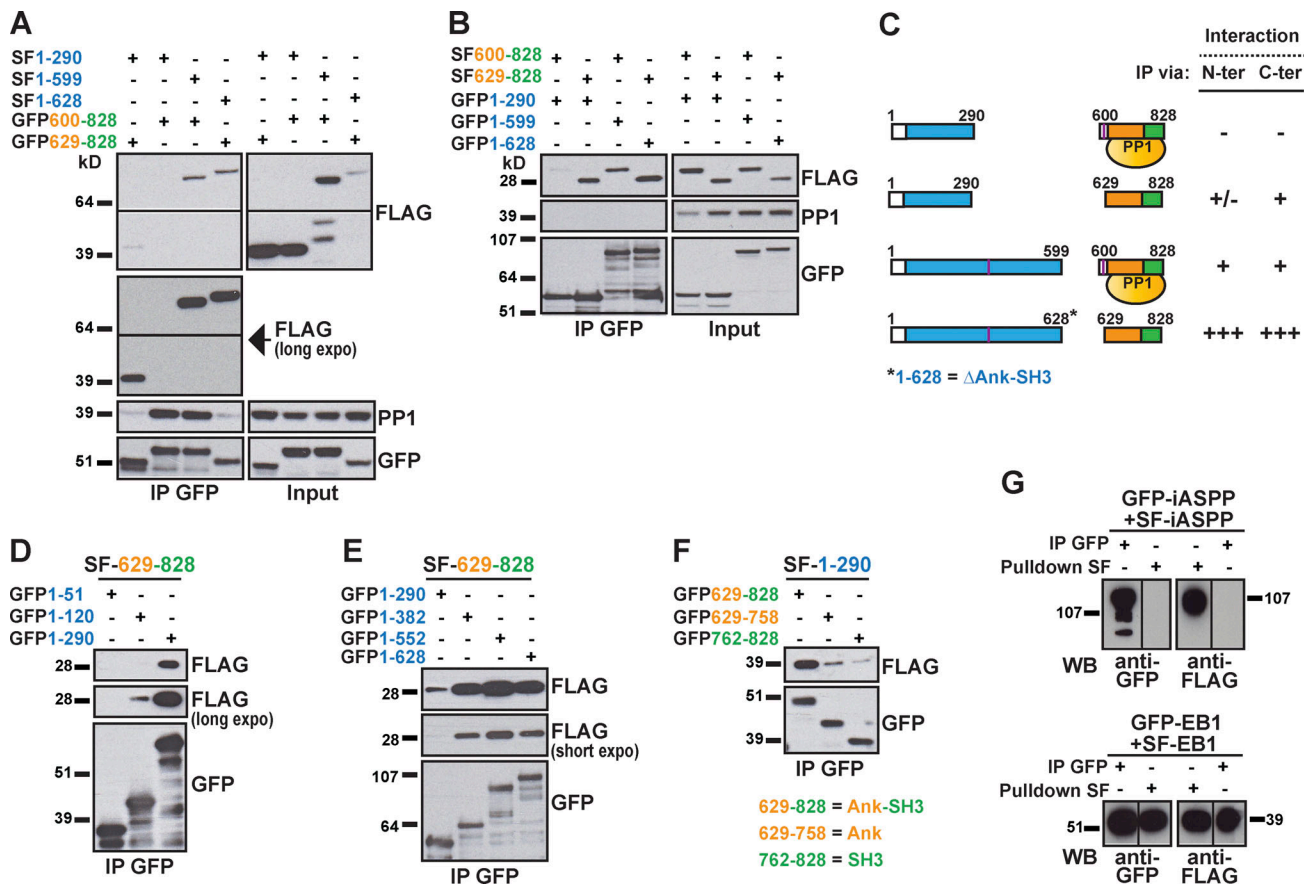


Figure 2. **Interaction of iASPP C-terminal (C-ter) region with iASPP N-terminal (N-ter) region is prevented upon PP1 binding.** (A–F) SF- and GFP-iASPP constructs were coexpressed in HEK293F cells before IP with GFP-Trap and WB analysis. Color code for the constructs corresponds to the functional domains as illustrated in Fig. 1 E. (A) IP was performed via iASPP C-terminal fragments. Note that SF1-628 is expressed at lower levels than SF1-599, which means that the efficacy of coprecipitation was much better for the pair GFP629–828/SF1-628 than for GFP600–828/SF1-599. (B) IP was performed via iASPP N-terminal fragments. (C) Summary of the IP results. (D and E) Characterization of the N-terminal sequences involved in the interaction with the C-terminal region. (F) Characterization of the C-terminal domains required for interaction with the N-terminal region. (G) iASPP does not form homodimers. Top: GFP- and SF-iASPP constructs were coexpressed before pulldown with GFP-Trap or Strep-Tactin beads and WB. Bottom: A similar experiment was performed using GFP- and SF-EB1 constructs. See also Fig. S1 E, expo, exposure.

**iASPP contributes to mitotic spindle positioning: Role of the SxIP motif**

Mitotic microtubules organize a symmetric spindle between centrosomes, which serves to capture and align chromosomes at the cell center. Astral microtubules transmit pulling and pushing forces, generated by cortical complexes, to the mitotic spindle to facilitate spindle positioning. We evaluated the contribution of iASPP to mitotic spindle organization in HeLa cells, which spontaneously align their spindle parallel to the substratum (di Pietro et al., 2016), using siRNA-mediated knockdown (Fig. S1 F). Microscopic examination revealed that upon iASPP knockdown, the mitotic spindle was often shifted to one side of the cell instead of being positioned at the cell center (Fig. 3 A). We measured the pole-to-cortex distance on either side of the spindle (Fig. 3 B and Fig. S2 A). While the shorter pole-to-cortex distance (d1) remained unchanged, the larger pole-to-cortex distance (d2) was significantly increased upon iASPP silencing (Fig. S2 A). As the pole-to-cortex distance could vary with cell size, we evaluated the mitotic spindle shift (d2-d1), which should be close to zero for centered spindles independently of cell size. In control

cells, d1 and d2 distribution was largely overlapping (Fig. S2 B), and the average spindle shift was close to 1 μm (Fig. 3 B). iASPP silencing induced a much larger shift of the spindle of ~3 μm (Fig. 3 B and Fig. S2 B). As a change in the size of the hemispindles might be a confounding factor, we also measured the cortex-to-metaphase plate distances (D1 and D2) and observed a similar shift upon iASPP knockdown (Fig. 3 B, right). Altogether, these analyses indicate that iASPP is involved in the proper centering of the spindle in the metaphase cell.

To investigate the respective contribution of iASPP-EB1 and iASPP-PP1 interactions to spindle positioning, we stably expressed iASPP constructs (Fig. 3 C) mutated in specific motifs and domains in HeLa cells. Expression of iASPP-SRNN, defective for EB1 binding, induced a large shift in mitotic spindle positioning (Fig. 3 D). Cells expressing iASPP-RARA, defective for PP1 binding, displayed appropriately positioned spindles, clearly showing that PP1 binding is not required for this function. Intriguingly, iASPPΔAnk-SH3, which showed strongly increased EB1 binding, was also defective for mitotic spindle centering, suggestive of a negative impact of excessive EB1 binding. These

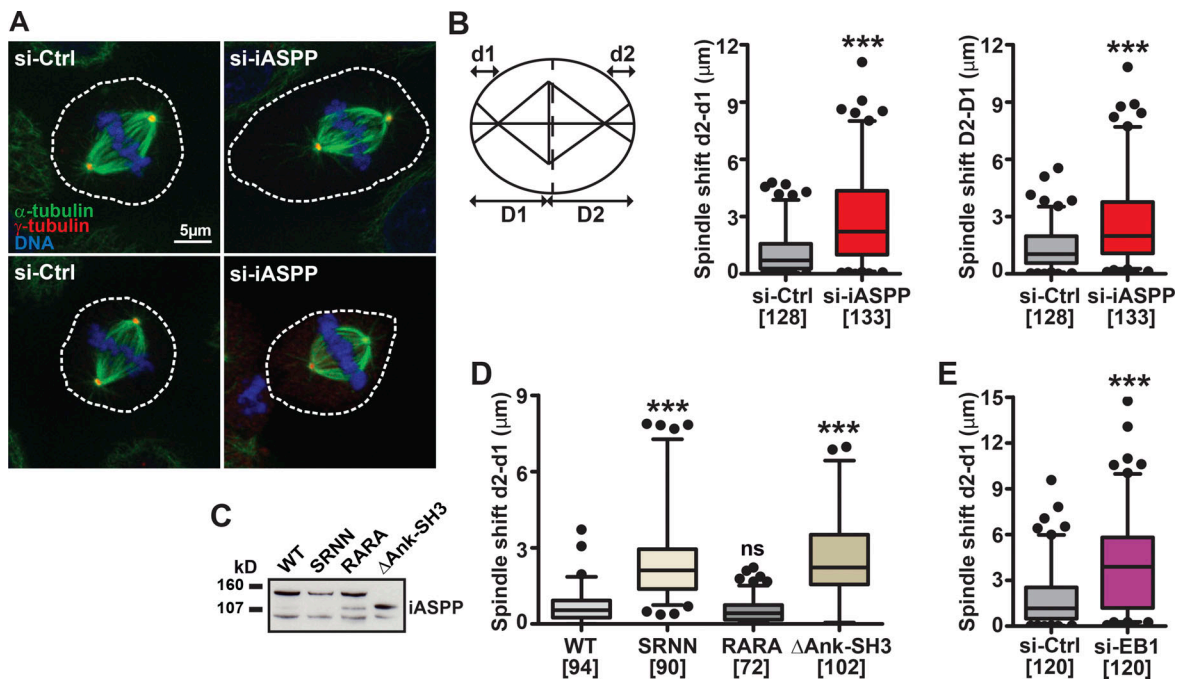


**Figure 3. iASPP is required for mitotic spindle positioning in metaphase, via EB1. (A and B)** HeLa cells were transfected with control (si-Ctrl) or iASPP targeting (si-iASPP) siRNA. Mitotic spindle, centrosomes, and chromosomes of metaphase HeLa cells were visualized by IF and DAPI staining (A). Mitotic spindle shift was calculated by comparing the pole-to-cortex (d1, d2) or metaphase plate-to-cortex (D1, D2) distances on either side of the spindle (B). Data are represented as box-and-whiskers plots with boxes showing 25th percentile, median, and 75th percentile and whiskers indicating the fifth and 95th percentiles. **(C and D)** Stable expression of GFP-iASPP constructs in HeLa cells was verified by WB (C) and spindle positioning quantified as above (D). **(E)** HeLa cells were transfected with Ctrl or EB1 (si-EB1) targeting siRNA and spindle shift calculated as above. Data are collected from three independent experiments. The number of cells analyzed is indicated between brackets. The unpaired two-tailed *t* test with Welch correction was used to determine if the difference was significant between data groups. \*\*\*, *P* < 0.001.

results strongly suggest that iASPP-EB1 interaction is critical for mitotic spindle positioning. Accordingly, EB1 silencing (Fig. S1 F) induced a strong shift of the mitotic spindle (Fig. 3 E).

**Myo1c is a partner of iASPP involved in spindle positioning**

To understand the mechanism whereby iASPP controls mitotic spindle positioning, we performed a systematic search for iASPP partners via GFP pulldown and mass spectrometry (MS) analysis as described before (Bouguenina et al., 2017), focusing specifically on proteins known to associate with the actomyosin cortex (Biro et al., 2013; Fig. 4 A). Among these, the main iASPP partner was Myo1c (Fig. 4 B), a class 1 myosin molecular motor. This was of particular interest since Myo1c is an actomyosin-associated protein (Fig. S1 G) involved in regulating membrane and cortical mechanics (McIntosh and Ostap, 2016). We observed that, similarly to EB1, Myo1c displayed stronger binding to C-terminally truncated iASPP (Fig. 4 C). iASPP disordered region was the main contributor to Myo1c binding (Fig. 4 C, right). We thus evaluated whether concomitant Myo1c and EB1 interaction with iASPP disordered region was possible: we observed that increasing Myo1c expression led to increased iASPP-Myo1c association and to reduced iASPP-EB1 interaction (Fig. 4 D), indicating that Myo1c and EB1 compete for binding iASPP.

Importantly, depletion of Myo1c (Fig. S1, F and G) induced a defect in spindle centering comparable to the one induced by iASPP knockdown (Fig. 4 E). In contrast, silencing of NuMA

(Fig. S1 F), a protein of the mitotic cortex important for mitotic spindle orientation (di Pietro et al., 2016), did not affect spindle centering. Thus, both iASPP and its cortical partner Myo1c contribute to mitotic spindle positioning.

**iASPP and Myo1c contribute to microtubule capture**

For a better understanding of the events that lead to mitotic spindle shift in iASPP- and Myo1c-silenced cells, we implemented a comprehensive reconstitution of the spindle and astral microtubule network of metaphase HeLa cells. Microscopic observations suggested that upon iASPP or Myo1c knockdown, astral microtubules failed to extend to the polar cortex on one side of the spindle, while still reaching the polar cortex on the other side (Fig. 5 A). Since astral microtubules are an essential relay of forces exerted by cortical molecular motors, which allow direct spindle orientation and positioning, it was important to document this observation further. Because the high density of astral microtubules prevented the accurate quantification of individual microtubules, we choose to quantify the number of EB1-labeled microtubule plus-ends that reached the cell periphery in different quadrants of the cells (Fig. 5 B). Astral microtubules extended in all directions but contacted the cell periphery mostly at the polar cortexes, with a slight dissymmetry, one polar cortex showing more microtubule ends than the other (Fig. S3 A). Microtubule ends at the lateral cortex were less frequent and were distributed symmetrically (Fig. S3 A).

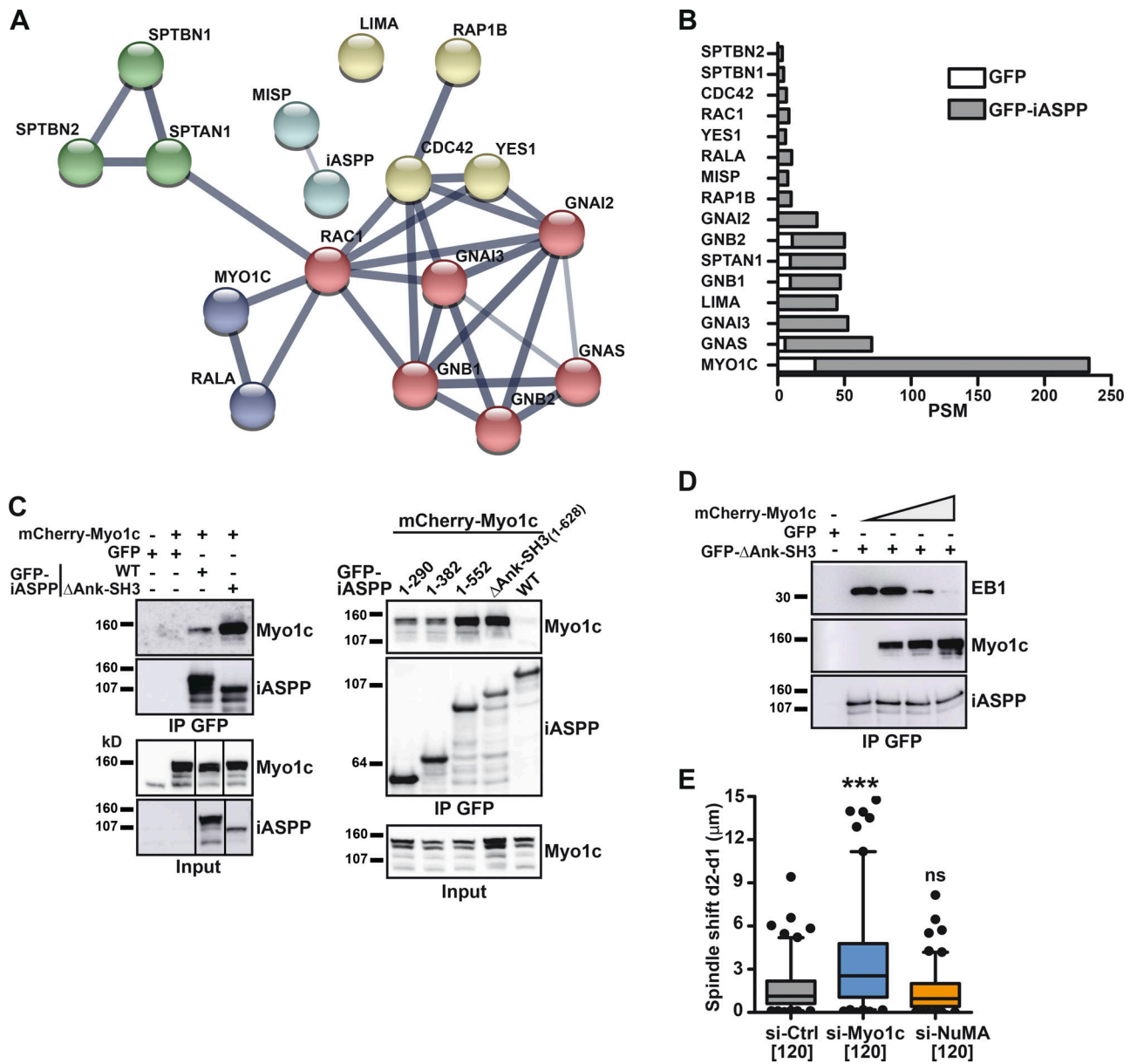
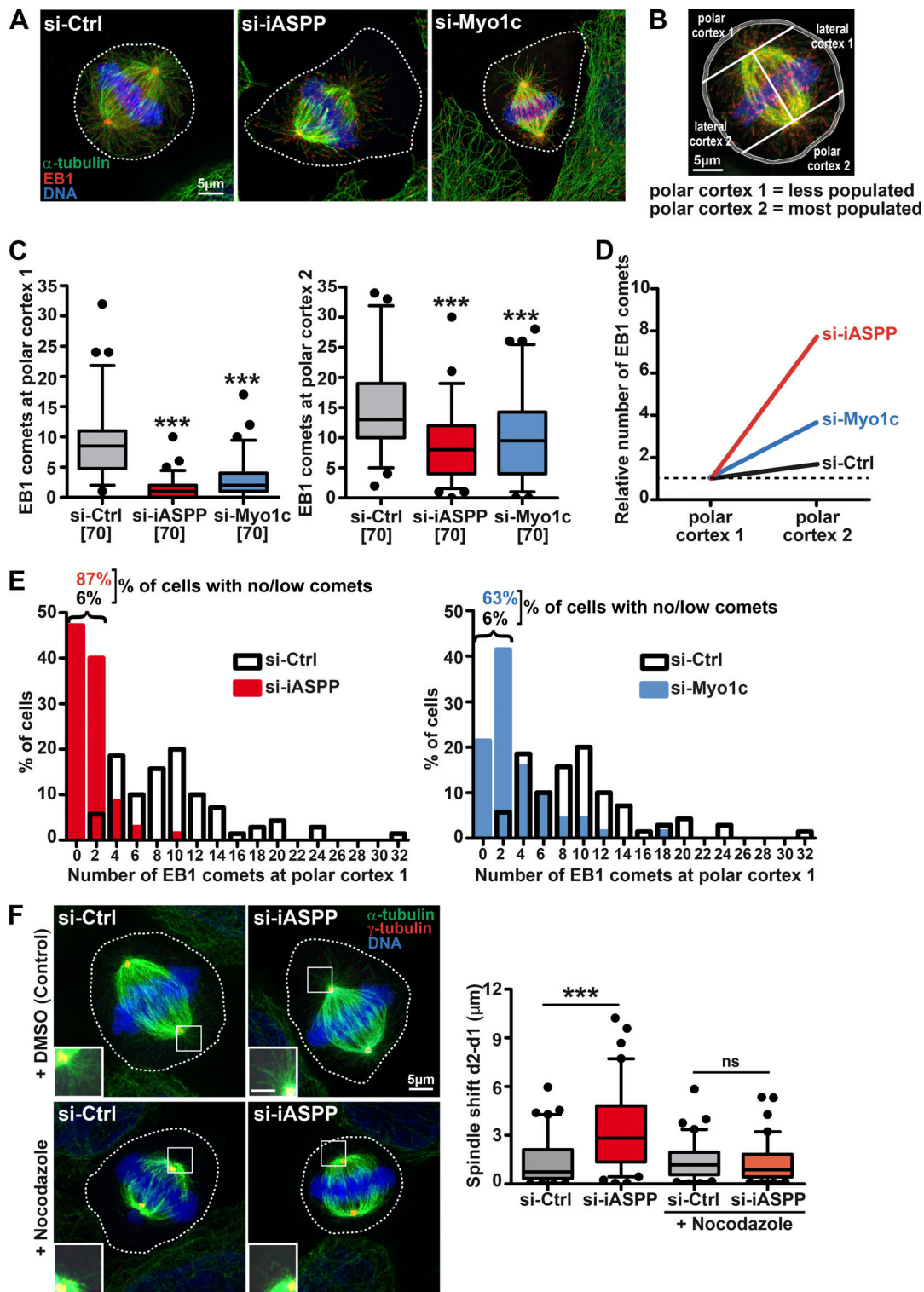


Figure 4. **Myo1c is a partner of iASPP required for mitotic spindle positioning in metaphase.** (A and B) GFP-iASPP was pulled down by GFP-Trap from SKBr3 cells stably expressing a C-terminally truncated GFP-iASPP. iASPP-associated proteins were identified by MS, and cortical proteins are displayed as a protein interaction network (STRING database 11.0; A) or as a bar graph of the number of peptide spectrum matches (PSM) identified in the GFP or GFP-iASPP pulldown (B). (C and D) GFP-iASPP constructs and mCherry-Myo1c were coexpressed before GFP pulldown and WB analysis. In D, increasing amounts of mCherry-Myo1c were expressed. Increasing Myo1c interaction correlates with decreasing EB1 binding. (E) HeLa cells were transduced with control (si-Ctrl), Myo1c (si-Myo1c), or NuMA (si-NuMA) targeting siRNA, and spindle shift was calculated as above. Data are from three independent experiments. The number of cells analyzed is indicated between brackets. The unpaired two-tailed *t* test with Welch correction was used to determine if the difference was significant between data groups. \*\*\*, *P* < 0.001.

We found that iASPP or Myo1c silencing induced a drop in the number of microtubule ends that reached the cell periphery (Fig. 5 C and Fig. S3 B). This effect was more pronounced at one polar cortex than at the other, resulting in a strikingly aggravated asymmetry in the number of astral microtubules that reached the polar cortex on either side of the spindle (Fig. 5 D). In fact, the quantification confirmed that upon iASPP or Myo1c knockdown, a large majority of cells had few or no comets at one polar cortex (Fig. 5 E) while retaining a

good number of microtubules at the opposite polar cortex (Fig. S3 C). Of note, this did not result from a reduction in the number of astral microtubules formed from the pole, since we measured that astral microtubule density remained equally distributed on either side of the spindle in knockdown cells (Fig. S3, D and E). Thus, spindle positioning defect might be the consequence of unbalanced forces generated by astral microtubules (Kern et al., 2016). Accordingly, upon specific elimination of astral microtubules by short treatment of the





**Figure 5. iASPP and Myo1c silencing leads to asymmetrical astral microtubule capture.** HeLa cells were transfected with control (si-Ctrl), iASPP (si-iASPP), or Myo1c (si-Myo1c) siRNA. **(A)** Microtubules, microtubule plus-ends, and chromosomes were visualized by confocal microscopy: representative maximum-image projections are shown. **(B–E)** The number of EB1 comets that reached a 2- $\mu$ m-wide strip drawn along the cell membrane (B) was determined. The number of comets at the “less-populated” polar cortex and the “most-populated” polar cortex was determined. Data from three independent experiments are represented: as box-and-whiskers plots (C); as mean cortical comet number normalized to polar cortex 1 (dashed line) to illustrate the asymmetry of microtubule capture between the two polar cortices (D); and as histograms of cell distribution according to cortical comet number at polar cortex 1, to illustrate very low or absent microtubule capture on one side of the spindle (E). **(F)** HeLa cells were treated with a low concentration of nocodazole (40 nM) for 60 min to induce depolymerization of astral microtubules before image acquisition. Left: Microtubules, centrosomes, and chromosomes of metaphase cells were visualized by IF. Inserts: zoomed images of the boxed regions; scale bar is 10  $\mu$ m. Right: Analysis of spindle shift as in Fig. 3. The unpaired two-tailed *t* test with Welch correction was used to determine if the difference was significant between data groups. \*\*\*, *P* < 0.001.

cells with low doses of nocodazole, iASPP-silenced cells recovered a centrally positioned spindle (Fig. 5 F).

### iASPP and Myo1c are required for mitotic cell rounding and cortex stiffening

Upon transition to mitosis, cells disassemble focal adhesions, detach from the substratum, and round up because of increased cortical tension (Ramkumar and Baum, 2016). Unexpectedly, we observed that iASPP and Myo1c-silenced mitotic cells were not spherical, but were distorted and flatter than control cells (Fig. 6, A and B), often filling up the space between interphase cells. We measured the shape and circularity of control and knockdown cells (Fig. 6 C). The shape ratio (i.e., the largest cell diameter divided by the width) was close to 1 in control and NuMA-depleted cells, reflecting the fact that they were mostly round. In contrast, the shape ratio was significantly higher in both iASPP and Myo1c knockdown cells (Fig. 6 D), and cell circularity diminished (Fig. S4 A). Interestingly, cells expressing iASPP defective for EB1 binding also failed to round up, while cells defective for PP1 binding were close to normal (Fig. 6 E), showing that, similar to what we have observed for mitotic spindle positioning, EB1 binding is central for mitotic rounding. PP1 binding is not critical for this function but could have a regulatory function.

The lack of cell rounding could be the consequence of inappropriate disassembly of cell-substrate adhesion sites (Dao et al., 2009). However, we observed that mitotic iASPP knockdown cells disassembled both focal adhesions and actin stress fibers (Fig. S4 B). We thus suspected that defective rounding might be due to insufficient stiffening of the cortex (Kunda et al., 2008). Recent studies evaluated the biomechanical properties of mitotic HeLa cells by atomic force microscopy (AFM). Most of these used wedged cantilevers, which gave access to global cellular parameters such as intracellular pressure and surface tension (Taubenberger et al., 2020; Toyoda et al., 2017; Chugh et al., 2017). As we wanted to analyze more specifically the mechanical properties of the cortex, we preferred indentation AFM, measuring the response of the cells to local deformation by a cantilever equipped with a pyramidal probe: since the indentation depth is limited, the response to deformation is dominated by the cell cortex. Synchronization of AFM with real-time microscopy (Cazaux et al., 2016) allowed identifying live metaphase cells (Fig. S4 C). The AFM force-indentation curves were fitted with the Hertz model to derive an apparent Young's modulus (Fig. S4 D). HeLa cell elasticity is typically in the kPa range (Sadoun and Puech, 2017; Shimizu et al., 2012; Chen et al., 2021). We found that when iASPP or Myo1c was silenced, mitotic cell stiffness was greatly decreased, showing a 40% and 60% drop in Young's modulus, respectively (Fig. 6 F). Thus, iASPP and Myo1c are important contributors to mitotic cell rigidity. We then wanted to verify that low cortical tension was actually the cause of abnormal cell rounding. We therefore used overexpression of constitutively active ERM proteins as the means to strengthen cortical tension (Kunda et al., 2008; Liu et al., 2012). We observed that expression of phosphomimetic moesin or ezrin in iASPP defective cells significantly restored rounding of mitotic cells (Fig. 6 G), confirming that defective mitotic cell rounding was indeed the consequence of low cortical tension.

Recent evidence suggests that modulating rounding or cortical rigidity has a direct impact on mitotic progression and chromosome segregation (Matthews et al., 2020; Serres et al., 2020; Carreno et al., 2008). Along this line, we observed that synchronized iASPP knockdown cells accumulated into mitosis (Fig. 5 H). Moreover, iASPP knockdown induced a moderate but significant increase in the proportion of cells that failed to properly align chromosomes in metaphase (Fig. 5 I), indicating that iASPP overexpression favors proper mitosis.

## Discussion

This study defines a novel function of iASPP in the control of mitotic cell rigidity with consequences on mitotic cell rounding and positioning of the mitotic spindle. This function depends on iASPP's newly identified partners, EB1 and Myo1c.

We propose that iASPP adopts variable supramolecular organizations, which depend on relative affinities for and local concentrations of its partners. From our experiments, iASPP does not generally form homodimers. This is probably the consequence of the low-affinity interaction between the N- and C-terminal fragments and the robust association of the C-terminal region to PP1. The affinity of PP1 for iASPP is in the low nanomolar range (Bertran et al., 2019). Considering that PP1 is expressed at much higher levels than iASPP [(PP1) = 2.8  $\mu$ M vs. (iASPP) = 31 nM in HeLa cells; Hein et al., 2015], it is likely that the bulk of iASPP is associated with PP1. While EB1 is expressed at a similar concentration as PP1 in HeLa cells (2.7  $\mu$ M), the affinity of EB1 for SxIP motif-harboring proteins is in the micromolar range (Buey et al., 2012), explaining why iASPP-PP1 is the major complex in the cytoplasm. However, EB1 is present at a much higher concentration at microtubule ends (Seetapun et al., 2012) and in a more favorable conformation for SxIP binding (Kanaba et al., 2013), explaining a possible recruitment of iASPP to EB1 at this particular location. Of note, even though it contains a validated SxIP motif, endogenous iASPP does not form comets at microtubule ends. This does not exclude that low amounts of iASPP interact with EB1 at microtubule ends or elsewhere transiently. Many other typical +-TIPs do not track microtubules when assessed at endogenous levels, the best example being CLASP1/2 (Stehbens et al., 2014; Hotta et al., 2010; Nakaya et al., 2013), which associates with the cell periphery. Similarly, immunofluorescence (IF) images of iASPP at endogenous levels of expression suggested encounters with EB1 in cortical areas and other undefined cytoplasmic locations (Fig. S1 B).

This work identifies Myo1c as a novel partner of iASPP, important for its function. Since our results indicate that EB1 and Myo1c cannot concomitantly bind iASPP, the association of iASPP with one or the other partner will be determined by their relative affinity and local concentration: iASPP is more susceptible to interact with EB1 at microtubule plus-ends where EB1 is concentrated and with Myo1c at the cortex, where this protein is enriched (Fig. S1 G). The relative affinity of EB1 and Myo1c for iASPP might be regulated during the cell cycle. A previous study suggests that iASPP is phosphorylated by cyclin B1-CDK1 mitotic kinase, which prevents iASPP N-terminal to C-terminal iASPP



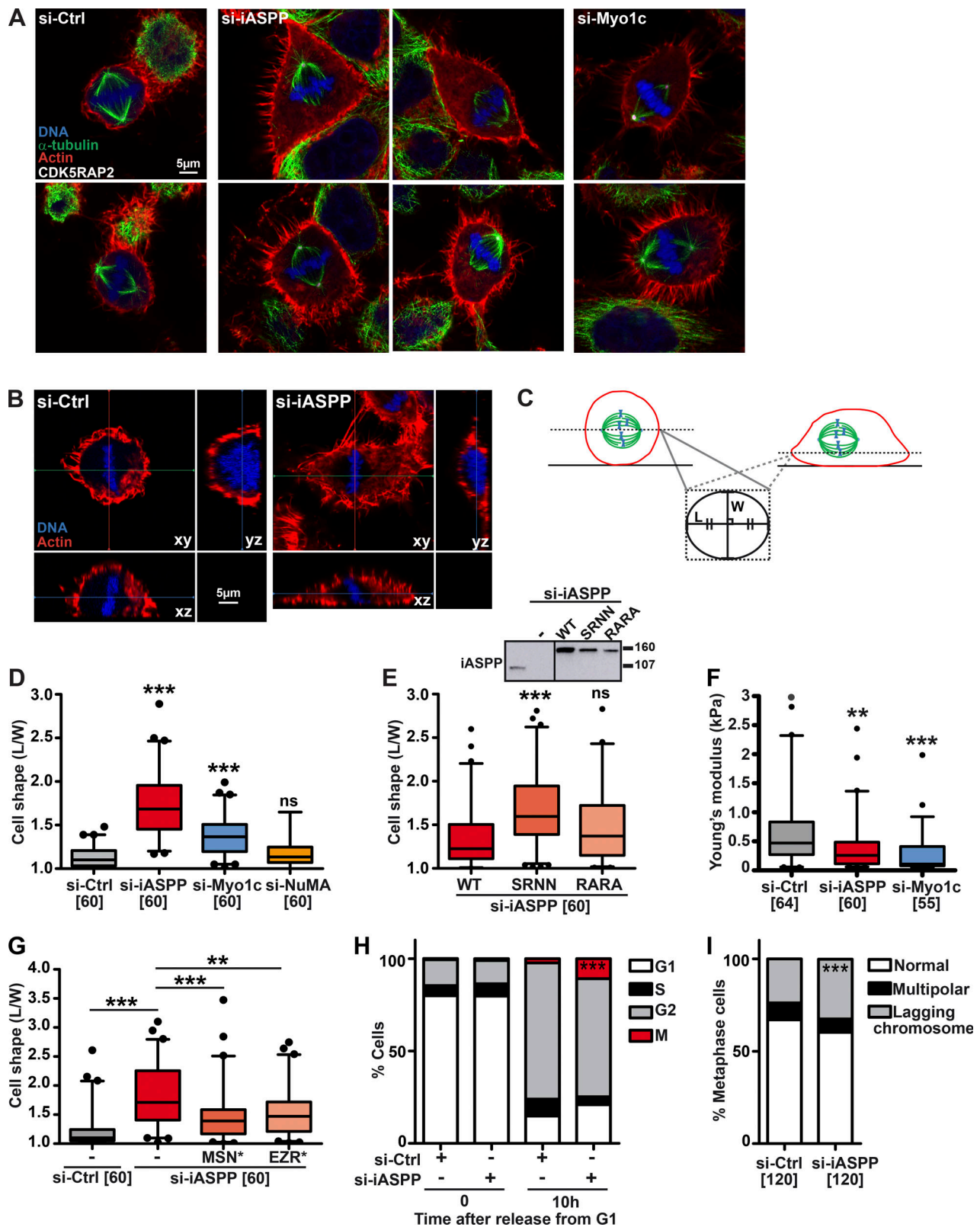


Figure 6. **iASPP and Myo1c silencing prevents rounding of mitotic cells and reduces cortical rigidity.** (A–I) HeLa cells were transfected with control (si-Ctrl), iASPP (si-iASPP), Myo1c (si-Myo1c), or NuMA (si-NuMA) siRNA and GFP-tagged iASPP-WT, -SRNN, or -RARA constructs (E) or GFP, GFP-tagged moesin T558D (MSN\*), or ezrin T567D (EZR\*; G) before labeling of microtubules, actin, centrosomes, and actin (except in H). (A and B) Representative confocal microscopy images are shown. (C, D, E, and G) Metaphase cell shape was quantified by measuring the ratio of the largest cell diameter (L) to the width (W) as shown in C. In E, the WB shows endogenous iASPP and GFP-iASPP construct expression levels. (F) Stiffness of live mitotic mCherry-H2B-expressing HeLa cells was measured by indentation AFM. The grey dot outlier (for si-Ctrl) is at 3.7 kPa. (H) Cells were released from G1 block, and the cell cycle was analyzed by FACS

after 0 and 10 h and the percentage of cells in each phase of the cycle presented. (I) The percentage of metaphase cells having more than two poles or showing retarded chromosomes that failed to align at the metaphase plate was determined. Data are collected from three independent experiments. The unpaired two-tailed *t* test with Welch correction was used to determine if the difference was significant between data groups. Data in F were collected from four or five experiments and analyzed with the Kruskal-Wallis test with Bonferroni adjustment. \*\*\*,  $P < 0.001$ ; \*\*,  $P < 0.01$ .

interaction (Lu et al., 2013). While we also observed that iASPP is heavily phosphorylated upon entry into mitosis (Fig. S5 A), in our hands, this did not disturb N-terminal to C-terminal interaction (Fig. S5 B) but interestingly decreased iASPP–EB1 interaction (Fig. S5 C). We can thus envision that iASPP binding to EB1 contributes to raise the concentration of iASPP at the cell periphery where, in turn, it will be able to encounter and interact with Myo1c (Fig. S1 B and Fig. S5 D). In this model, either defective binding to EB1 or excessive iASPP–EB1 interaction (as observed for the iASPP- $\Delta$ Ank-SH3 mutant; Fig. 1 F and Fig. 3 D) might prevent relocalization to Myo1c and thus be detrimental for iASPP cortical functions. How iASPP affects cortical rigidity remains to be solved, but as iASPP does not directly bind the membrane or actin, it could act by contributing to the regulation of Myo1c activity.

Mitotic cell rounding is the consequence of the loss of focal adhesions and increased intracellular pressure. This is accompanied by changes in mechanical properties, including cell surface tension and cortical stiffness. These changes depend on the composition and architecture of the contractile actomyosin cortex and on tight tethering of the cortex to the plasma membrane (Taubenberger et al., 2020). While several proteins have the ability to link the membrane to the actin cytoskeleton (such as spectrin in red blood cells and talin in *Dictyostelium discoideum* cells), ERM proteins are often considered critical in mitosis, since moesin was involved in cortical stiffening and cell rounding in S2 *Drosophila* cells (Carreno et al., 2008; Kunda et al., 2008). However, the picture is less clear in mammalian cells, as others (Machicoane et al., 2014) and our preliminary data (Fig. S4 F) indicate that ERMs are not essential for rounding of mitotic HeLa cells. Like ERMs, class 1 myosins are enriched at the plasma membrane and are capable of interacting both with the actin cytoskeleton via their motor domain and membranes via their tail homology domain. Structural studies show that class 1 myosins are extended and rather rigid molecules with the actin-binding domain at one end and the lipid-interacting domain at the other end (Jontes and Milligan, 1997; Lu et al., 2015), well suited for transducing tension forces while maintaining an ~20-nm gap, which is close to the estimated spacing between the membrane and the inner boundary of the cortex (Clausen et al., 2017). Class 1 myosins are important regulators of membrane tension and/or cortex rigidity in interphase brush border cells, fibroblasts, and macrophages (Nambiar et al., 2009; Venit et al., 2016; Barger et al., 2019). Our observations demonstrate that, similarly to moesin in S2 cells, Myo1c contributes to cortical stiffening and rounding of mitotic HeLa cells. iASPP has a similar contribution to mitotic cell rounding, but as it does not bind actin or the plasma membrane, its action is conceivably mediated by its partner Myo1c. It has been shown that upon increased calcium concentrations, Myo1c tail undergoes a major conformational change leading to higher flexibility (Lu et al.,

2015). It will be interesting to investigate whether iASPP binding affects Myo1c extended conformation in vitro using structural approaches and in vivo using fluorescence resonance energy transfer-based Myo1c tension sensors (Kannan and Tang, 2018). Alternatively, iASPP might contribute to microtubule targeting to the cell cortex, allowing the delivery of a protein regulating Myo1c conformation or activity.

It was proposed that a rigid and uniform cortex facilitates physical interactions between the plus-ends of astral microtubules and the actomyosin cortex, enabling the spindle to exert and sustain cortical forces for proper positioning of the mitotic spindle (Ramkumar and Baum, 2016). For instance, upon disturbance of cellular stiffness, cultured S2 metaphase cells failed to retract their margins, remained flat (Kunda et al., 2008), and displayed disturbed mitotic spindle positioning (Carreno et al., 2008), showing images strikingly similar to iASPP/Myo1c knockdown cells. Thus, abnormal astral microtubule attachment to the cortex and mitotic spindle mispositioning might be the consequence of cortex softening. This is supported by the observation that stiffening of the cortex via expression of constitutively active ERM restored symmetric spindle positioning in iASPP knockdown cells (Fig. S4 E).

The rounding of mitotic cells is a common feature that has been observed in many cell types in culture or in tissues. It has recently become appreciated that mitotic rounding, by ensuring that there is sufficient space to form and orient a mitotic spindle, facilitates successful cell division (Cadart et al., 2014). In contrast, it was shown that in flattened cells, the mitotic spindle cannot rescale to account for the altered geometry and is unable to efficiently capture chromosomes due to an upper limit in astral microtubule reach (Lancaster et al., 2013). In iASPP knockdown cells, even though the projected cell area was increased, the size of the spindle was not (Fig. S2 A). Although astral microtubules were not captured and remained distant from the cortex on one side, they did not extend beyond the usual length (Fig. S3 D). They are thus probably less efficient in reaching chromosomes dispersed in the extended cell area and contributing to the poleward movement of chromosomes that precedes congression of a subset of chromosomes (Maiato et al., 2017), explaining the increase in the proportion of cells that fail to align some chromosomes. The satisfaction of the spindle assembly checkpoint being conditioned to the attachment of all chromosomes, this might, in turn, lead to the observed prolonged stay in metaphase.

It was proposed that cancer cells could hijack pathways impacting actomyosin cortex properties to enable them to successfully round up and divide in different environments (Matthews and Baum, 2012). For instance, active Ras alters cell mechanics, enhances cell rounding, and contributes to prevent mitotic defects of breast cancer cells growing in a rigid environment (Matthews et al., 2020). By promoting cell rounding,

thus ensuring conditions favorable for the correct positioning of the spindle, iASPP might similarly contribute to the accurate segregation of chromosomes in the mechanically altered tumor environment (Levental et al., 2009; Nagelkerke et al., 2015; Brauchle et al., 2018).

## Materials and methods

### Cell lines

SKBr3 (American Type Culture Collection/LGC Standards), HEK293F (Thermo Fisher Scientific), and HeLa cells (a kind gift of P. Dubreuil, Centre de Recherche en Cancérologie de Marseille [CRCM], Marseille, France) were cultured in DMEM (Thermo Fisher Scientific) supplemented with 10% fetal bovine serum (Eurobio) at 37°C in a humidified atmosphere with 5% CO<sub>2</sub> and were checked regularly for mycoplasma contamination.

### Cell transfection

Plasmid transfection of HEK293F and HeLa cells was performed with Fugene HD (Promega), whereas SKBr3 cells were transfected using Fugene 6 (Promega), following the manufacturer's instructions. Transfection of siRNA was performed using Lipofectamine RNAiMax (Thermo Fisher Scientific) via the reverse transfection method. For ERM rescue experiments, HeLa cells were first transfected with iASPP siRNA and GFP or GFP-tagged active ezrin or moesin 24 h later. Cell lysate was collected 48–72 h later. Stable HeLa and SKBr3 cell lines were generated by transfection with the indicated iASPP constructs, selection with 1 mg/ml geneticin (Thermo Fisher Scientific), and sorting by flow cytometry. HeLa cell clones with comparable GFP-tagged construct expression levels were selected. The HeLa cell population expressing GFP- $\alpha$ -tubulin and mCherry-histone H2B constructs was selected successively with geneticin and 0.1 mg/ml hygromycin B.

### Endogenous protein split GFP-tagging

A split-GFP system (Leonetti et al., 2016) was used to insert a minimal tagging sequence (GFP11, the 11th  $\beta$ -strand of the superfolder GFP barrel  $\beta$ -barrel structure) at EB1 endogenous loci. HeLa cells expressing the complementary GFP1-10 fragment were generated by lentiviral integration from pHR-SFFV-GFP1-10 (a gift from B. Huang; Addgene plasmid #80409) and isolation of a clonal cell line. Homology-directed repair (HDR) donor templates and associate gRNAs were selected by the Alt-R CRISPR HDR Design Tool (Integrated DNA Technologies [IDT]) to allow insertion of GFP11 C-terminally to *MAPRE1* gene and (GFP11)<sub>7</sub> N-terminally to *PPP1R13L* gene. The following gRNA sequences were used: for EB1 gRNA1: 5'-CAAGAAGAGTATTAA CAGCC-3'; and for iASPP gRNA1: 5'-CTGGAATGCCTCGCTGTC CA-3', gRNA2: 5'-TGCCTCGCTGTCCATGGTGC-3'. GFP11 and (GFP11)<sub>7</sub> single-stranded DNA templates with 40 and 250 nucleotide homology arms were obtained from IDT and Genewiz, respectively. Ribonucleoprotein complex was prepared from AltR-Cas9 and gRNA (both from IDT) according to manufacturer's protocol and delivered together with the HDR template into HeLa<sup>GFP1-10</sup> cells by nucleofection (kit R; Lonza). Coexpression of GFP1-10 and GFP11 in the same cell allows

reconstitution of a functional GFP molecule. GFP-positive cells were sorted on a FACSAria III cytometer (BD Biosciences). Homogeneity of the subcellular distribution of GFP-tagged proteins in the cell population (and across the two populations generated from two independent gRNAs for iASPP-GFP) was verified by fluorescence microscopy. The ability of GFP-iASPP knock-in mitotic cells to round up was also verified.

### Plasmids and siRNA

pEGFP-C1 and pEGFP- $\alpha$ -tubulin was obtained from Clontech. pBabeD-mCherry-histone H2B was a kind gift from C. Lachaud (CRCM, Marseille, France). pDEST-EGFP-C1 and pDEST myc-BioID were derived from pEGFP-C1 and pcDNA3.1 mycBioID (a gift from K.J. Roux, Sanford Research, Sioux Falls, SD; Addgene plasmid #35700) to allow Gateway-based cloning. iASPP cDNA was amplified by PCR from pcDNA3V5iASPP (a gift from X. Lu, Ludwig Institute, Oxford, UK) and cloned into pDONRZeo. iASPP was subcloned into pDEST-EGFP-C1 in order to obtain GFP-tagged iASPP, pDEST/N<sup>-</sup>, or C-SF-TAP (a gift from C.J. Gloeckner, University of Tübingen, Tübingen, Germany) to obtain Strep- and FLAG-tagged iASPP (SF-iASPP), 2HA-pDEST-C or -N (a gift from M. Vartiainen, University of Helsinki, Helsinki, Finland; Addgene plasmid #118374) to obtain HA-tagged iASPP and pDESTmycBioID to obtain BirA-fused iASPP. iASPP point mutations (SRIP to SRNN and RARL to RARA) were produced by Quickchange site-directed mutagenesis (Agilent). Truncated forms of iASPP were generated by PCR amplification and cloned into pDONRZeo before integration into destination vectors. Plasmid-expressing human EB1 (EB1-EGFP JB 131) was a gift from T. Mitchison and J. Tirnauer, Harvard University, Boston, MA (Addgene plasmid #39299). EB1 was cloned into pDEST/N-SF-TAP in order to obtain EB1-SFII and into pcDNA3.1 MCS-BirA(R118G)-HA (a gift from K.J. Roux; Addgene plasmid #36047) to produce EB1-BirA. Myosin 1c-mCherry construct was a gift from P. Miklavc and M. Frick (Ulm University, Ulm, Germany). GFP-tagged active moesin (pHJ322) and ezrin (pHJ423) constructs were gifts from S. Shaw, National Institutes of Health, Bethesda, MD (Addgene plasmid #20677 and #20681).

The following siRNAs, selected with support vector machine siRNA Design Tool (Applied Biosystems) software and synthesized by Thermo Fischer Scientific, were used: iASPP-3044 (sense strand: 5'-GAAACUUUCCUUAAAUAATT-3'); Myosin 1c-1480 (sense strand: 5'-GGAUAUUUAUGGCUUUGAA-3'); NuMA-7297 (sense strand: 5'-GGAUCUUUUCUAAAUGUUA-3'); EB1-1262 (sense strand: 5'-UUAAAUACUCUUAAGGCA UTT-3'). ERM siRNA sequences were from Machicoane et al. (2014). An siRNA targeting the  $\beta$  galactosidase gene from *Escherichia coli* (LacZ; sense strand: 5'-GCGGCUGCC GGAAUUUACCTT-3') was used as negative control.

### Antibodies

The following antibodies were used for Western blotting (WB) and IF: anti- $\gamma$ -tubulin GTU88 (IF),  $\alpha$ -tubulin clone DM1A (IF+WB),  $\alpha$ -tubulin clone YL 1/2 (IF),  $\beta$ -actin clone AC15 (IF), GFP (WB), PPP1R13L HPA041231 (WB), myosin 1c HPA 001768 (IF, WB), FLAG M2 (WB) from Sigma-Aldrich; anti-mCherry (WB) and NuMA [EP3976] (WB) from Abcam; anti-iASPP



18590-1-AP (WB) from Proteintech and PCRP-PPP1R13L-2G4 (WB) from Developmental Studies Hybridoma Bank; anti-ERM #3142 (WB), anti-EB1 clone 5 (WB), and anti-HA clone 6E2 (WB) from Cell Signaling Technology; anti-EB1 KT51 (IF), myosin Ic (13; WB), PPI $\alpha$  (C-19; WB) from Santa Cruz Biotechnology; anti-CDK5RAP2, A300-554 (IF) from Bethyl; anti-Phospho-Histone H3 (Ser10) from Millipore (WB); and anti-GFP JL-8 from Clontech (for GFP1-10, WB). GFP-Trap was from Chromotek, anti-HA agarose conjugated beads, tetramethylrhodamine isothiocyanate (TRITC)-phalloidin from Sigma-Aldrich, and Strep-Tactin beads from IBA.

### WB, protein pulldowns, and MS analysis

Cells were lysed in a Nonidet P-40-based lysis buffer (10 mM Tris, pH 7.5, 150 mM NaCl, 0.5 mM EDTA, and 0.5% NP-40) supplemented with protease and phosphatase inhibitors (Roche). When indicated, HeLa cells were treated with 10  $\mu$ M nocodazole for 16 h before cell lysis. Cells expressing the tagged constructs were lysed, and GFP, HA, or Strep-iASPP pulldowns were performed using GFP-Trap, anti-HA agarose, or Strep-Tactin beads (Daou et al., 2014; Bouguenina et al., 2017). Proximity biotinylation was essentially as described (Bouguenina et al., 2017; Roux et al., 2012). Briefly, cells expressing EB1-BirA or BirA-iASPP were treated overnight with 50  $\mu$ M biotin and were lysed in denaturing buffer (50 mM Tris, pH 7.4, 500 mM NaCl, 0.4% SDS, 2% Triton X-100, 5 mM EDTA, and 1 mM DTT) supplemented with protease and phosphatase inhibitors. Biotinylated proteins were isolated by incubating the cell lysates with Avidin-coated beads (Thermo Fisher Scientific) for 1 h at 4°C. For WB, samples were run on Novex NuPAGE Bis-Tris 4–12% gels using a MOPS-based running buffer. To detect gel-retarded phosphorylated iASPP, cells were washed in salt-free isotonic buffer and lysed in 7 M urea, 2 M thiourea, 4% CHAPS, 20 mM spermine, and 40 mM DTT buffer and run on 6% polyacrylamide gels. For 2D gels, samples were run on pH4–pH7 isoelectric focusing gels (GE Healthcare) for the first dimension, reduced and alkylated, and run on Novex 4–12% gels for the second dimension. Proteins were transferred onto nitrocellulose membranes, incubated with the primary antibodies listed above and secondary antibodies coupled to HRP, and detected by chemiluminescence. Quantification of WB was performed with Image J software. For MS analysis, GFP pulldown samples from SKBr3 cells stably expressing a spontaneously C-terminally truncated GFP-iASPP were analyzed by liquid chromatography–tandem MS/MS in an LTQ-Orbitrap-Velos (Thermo Electron) online with a nanoLC Ultimate 3000 chromatography system (Dionex). Protein identification and relative intensity-based label-free quantification were processed using Progenesis liquid chromatography–MS software, version 4.1 (Nonlinear Dynamics) as described previously (Daou et al., 2014). Only proteins identified with at least two peptides in two out of four independent replicates were selected. Among these, proteins associated with the cell cortex were identified through a literature search.

### Microscopy and flow cytometry

HeLa cells transfected with the indicated siRNA were grown on glass coverslips coated with 25  $\mu$ g/ml rat-tail collagen I for 72 h. When indicated, nocodazole at a final concentration of 40 nM

was added to the culture medium for 1 h. For IF, cells were fixed either with methanol containing 1 mM EGTA at  $-20^{\circ}\text{C}$  for 5 min, followed by 4% formaldehyde in PBS for 15 min at room temperature or with 4% formaldehyde and 3% sucrose in PBS for 20 min at  $37^{\circ}\text{C}$ . After permeabilization with 0.2% Triton in PBS for 10 min, immunolabeling was performed with antibodies against target proteins and secondary antibodies coupled to Alexa Fluor 488, 546, 594, or 647 (Jackson ImmunoResearch), and DNA was counterstained with DAPI (Sigma-Aldrich). Images were acquired on a Zeiss structured light ApoTome microscope equipped with a 63 $\times$ /1.4 plan Aplan objective and an AxioCam MRC5 camera using AxioVision software or a Zeiss LSM880 META confocal microscope equipped with a 63 $\times$ /1.46 plan Aplan objective and a GaAsP detector using Zen software.

For flow cytometry cell cycle analysis, cells were synchronized in G1 by a double block with 2 mM thymidine, collected 0 and 10 h after thymidine wash off, and permeabilized with 0.2% Triton in PBS. After the addition of anti-phospho-histone H3 antibody and anti-rabbit IgG coupled to secondary Alexa Fluor 647 to label mitotic cells, cells were resuspended in a solution of 40  $\mu$ g/ml propidium iodide/RNase A (Sigma-Aldrich) for 30 min in the dark at  $37^{\circ}\text{C}$ . DNA content and histone H3 phosphorylation were determined with an LSRFortessa flow cytometer (BD Biosciences), and cell cycle was analyzed using FlowJo V10 Software.

### Analysis of microscopy images

To determine spindle position in the xy plane, microtubules, centrosome, and DNA were labeled as indicated in Materials and methods to identify mitotic cells. Images were acquired with a Zeiss structured light ApoTome microscope. Only metaphase cells with both poles in the same focus plane were quantified, to disregard effects on spindle orientation. Cell size, mitotic spindle size, cortex-to-pole distances ( $d_1$  and  $d_2$ ), and cortex-to-metaphase plate distances ( $D_1$  and  $D_2$ ) were measured via Image J software in three independent experiments. The number of counted cells is indicated.

Astral microtubule plus-ends were identified thanks to EB1 labeling and quantified on z-stack image projections (40  $\times$  0.2- $\mu$ m-thick sections). Astral microtubule EB1 comets that entered a 2- $\mu$ m-wide strip drawn along the cell periphery, as indicated in Fig. 5, were counted in three independent experiments. Astral microtubule density was determined by measuring  $\alpha$ -tubulin total fluorescence minus spindle fluorescence after correcting for background fluorescence, as described previously (Bouguenina et al., 2017). To evaluate metaphase cell morphology, cells were labeled with anti- $\beta$ -actin or TRITC-phalloidin, anti- $\alpha$ -tubulin and anti-CDK5RAP antibodies, and DAPI before acquisition of 0.42- $\mu$ m-thick sections encompassing the entire cell. For ERM rescue experiments, only GFP-positive cells were included in the analysis. Images were acquired with a Zeiss confocal LSM880 META microscope, using a 63 $\times$  objective and a numeric zoom of 3.5. The largest cell diameter ( $L$ ) and related width ( $W$ ) were determined with Zen software. Circularity was measured in independent experiments: 0.25- $\mu$ m-thick sections were collected with a ZEISS Axio Observer Z1 microscope equipped with a Yokogawa CSU-X1A

head and a plan Apochromat 63×/1.46, and cytosolic  $\alpha$ -tubulin immunostaining was used to define cell limits using ImageJ particles analysis tool: maximum projection images, blurred with the Gaussian filter (sigma = 2 pixels), were used for thresholding, producing a binary image. A 150-pixel<sup>2</sup> size filter was applied before analysis of cell area, perimeter, and circularity [ $4\pi(\text{area})/(\text{perimeter}^2)$ ].

### AFM

EGFP-tubulin/mCherry H2B-HeLa cells were transfected with the indicated siRNA, plated on collagen I-coated glass-bottom FluoroDishes (WPI), and synchronized by a single 2-mM thymidine treatment. AFM measurements were performed in serum-free DMEM 12–14 h after thymidine washout. Details of the setup have been described elsewhere (Cazaux et al., 2016; Sadoun and Puech, 2017). In short, measurements were conducted with an AFM (Nanowizard I; JPK Instruments/Bruker) mounted on an inverted microscope (Zeiss Axiovert 200) with a CellHesion stage and a PetriDish Heater (JPK Instruments/Bruker). The setup was used in AFM force mode (15- $\mu$ m head piezo on, stage off) and in closed loop, constant-height feedback mode. The sensitivity of the optical lever system was calibrated on the Petri dish glass substrate; the cantilever (Bruker MLCT-bio C) spring constant was determined using the thermal noise method, thanks to JPK SPM software routines, at the start and at the end of each experiment. Spring constants were found to be consistently close to the manufacturer's nominal values (10 pN/nm). Bright-field images and/or fluorescence images were acquired with 10× or 40× NA 0.75 lenses, a CoolSnap HQ2 camera (Photometrics), and a four-diode Colibri2 (Zeiss) setup with suitable multiband filter sets (Cazaux et al., 2016).

The AFM tip was positioned over the center of mitotic cells (identified by morphology and/or organization of the mitotic spindle). A minimum of five force curves were gathered for each cell with a maximal pressing force of 500 pN, a pushing (and pulling) speed of 2  $\mu$ m/s, and an acquisition frequency of 2,048 Hz, making sure that cells were not moving during the indentation measurements with the optical microscope. Data from four to five experiments were collected and pooled.

### AFM data processing

Using custom-made Python-scripts and JPK-DP data processing software (JPK Instruments/Bruker), force curves were processed. We corrected for baseline offset and tilt and calculated tip sample separation before applying a fit based on the Hertz model for a square-based pyramid (Sadoun and Puech, 2017). We took care to keep the fitted indentation smaller than the minimum manufacturer-reported tip height (<2  $\mu$ m) and to verify by eye the goodness of the detection of the contact point for each curve. If the fit appeared to be bad quality, the corresponding force curve was rejected from the analysis. We then obtained for each processed curve a Young modulus (in Pa), calculated the mean Young modulus per cell, and plotted the distribution of the cell's Young moduli per experimental condition. The higher the value of Young modulus is, the stiffer the cell is.

### Statistical analysis

All experiments were performed at least three times independently. Statistical analyses were performed using GraphPad

Prism. The unpaired two-tailed *t* test with Welch correction was used to determine if the difference was significant between data groups. Data distribution was assumed to be normal, but this was not formally tested. For AFM analysis, R asbio package (<https://www.r-project.org/>) was used and analyzed with Kruskal-Wallis test with Bonferroni adjustment and verified using GraphPad Prism. Data are represented as box-and-whiskers plots, with boxes showing 25th percentile, median, and 75th percentile, and whiskers indicating the fifth and 95th percentiles. P values are indicated as \*, *P* > 0.05; \*\*, *P* < 0.01; and \*\*\*, *P* < 0.001.

### Online supplemental material

Fig. S1 shows images of endogenously tagged EB1 and iASPP and coprecipitation of endogenous GFP-tagged iASPP and EB1, the contribution of specific iASPP domains to PP1 binding, and the inability of HA- and FLAG-tagged iASPP to coprecipitate. It also shows the efficiency of the various siRNAs used in the study and data to confirm Myo1c cortical localization. Fig. S2 shows additional data on the effect of iASPP siRNA on spindle positioning and pole-to-cortex distance. Fig. S3 shows a complement of data on the effect of iASPP knockdown on microtubule capture at the cortex, including the lack of impact on astral microtubule nucleation. Fig. S4 shows the effect of iASPP siRNA on mitotic cell circularity, focal adhesions, and stress fibers. It also shows that ERMs do not contribute to mitotic rounding but that overexpressed active ERMs restore mitotic spindle positioning. It illustrates how AFM data were acquired. Fig. S5 shows that nocodazole treatment induces iASPP phosphorylation visualized as gel-retarded bands on 1D and 2D gels, and the impact of iASPP phosphorylation on N-terminal region–C-terminal region, iASPP–EB1, and iASPP–Myo1c interactions. It also presents a graphical summary.

### Acknowledgments

We thank M. Rodrigues (CRCM Microscopy and Scientific Imaging Platform) and M. Richaud (CRCM Cytometry Platform) for support and H. Bouguenina for generating preliminary results. We thank B. Huang, C. J. Gloeckner, X. Lu, P. Miklavc and M. Frick, T. Mitchison and J. Tirnauer, K.J. Roux, S. Shaw, and M. Vartiainen for sharing plasmids.

This work was supported by Agence Nationale de la Recherche grant ANR-16-CE11-0008. A. Mangon was supported by a Ministère de l'Enseignement Supérieur et de la Recherche Fellowship. The Marseille Proteomics core facility was supported by Infrastructures Biologie Santé et Agronomie, Plateforme Technologique Aix-Marseille, Canceropôle PACA, Région Sud Provence-Alpes-Côte d'Azur, Fonds Européen de Développement Régional, and Plan Cancer. CRCM Microscopy and Scientific Imaging Platform was supported by Fonds Européen de Développement Régional.

The authors declare no competing financial interests.

Author contributions: A. Mangon: investigation, formal analysis; writing–original draft. D. Salaün, M. Lala Bouali, M. Kuzmić, S. Thuault, S. Quitard: investigation, formal analysis. D. Isnardon: methodology, formal analysis. S. Audebert: methodology,

investigation, formal analysis. P.-H. Puech: methodology, investigation, formal analysis. P. Verdier-Pinard: conceptualization, formal analysis, investigation, supervision. A. Badache: conceptualization, formal analysis, funding acquisition, supervision, writing—original draft, with review and editing by all the authors.

Submitted: 1 December 2020

Revised: 3 August 2021

Accepted: 19 September 2021

## References

- Akhmanova, A., and M.O. Steinmetz. 2008. Tracking the ends: a dynamic protein network controls the fate of microtubule tips. *Nat. Rev. Mol. Cell Biol.* 9:309–322. <https://doi.org/10.1038/nrm2369>
- Barger, S.R., N.S. Reilly, M.S. Shutova, Q. Li, P. Maiuri, J.M. Heddeleston, M.S. Mooseker, R.A. Flavell, T. Svitkina, P.W. Oakes, et al. 2019. Membrane-cytoskeletal crosstalk mediated by myosin-I regulates adhesion turnover during phagocytosis. *Nat. Commun.* 10:1249. <https://doi.org/10.1038/s41467-019-09104-1>
- Bergamaschi, D., Y. Samuels, N.J. O'Neil, G. Trigiant, T. Crook, J.K. Hsieh, D.J. O'Connor, S. Zhong, I. Campargue, M.L. Tomlinson, et al. 2003. iASPP oncoprotein is a key inhibitor of p53 conserved from worm to human. *Nat. Genet.* 33:162–167. <https://doi.org/10.1038/ng1070>
- Bertran, M.T., S. Mouilleron, Y. Zhou, R. Bajaj, F. Uliana, G.S. Kumar, A. van Drogen, R. Lee, J.J. Banerjee, S. Hauri, et al. 2019. ASPP proteins discriminate between PP1 catalytic subunits through their SH3 domain and the PP1 C-tail. *Nat. Commun.* 10:771. <https://doi.org/10.1038/s41467-019-08686-0>
- Biro, M., Y. Romeo, S. Kroschwald, M. Bovellan, A. Boden, J. Tcherkezian, P.P. Roux, G. Charras, and E.K. Paluch. 2013. Cell cortex composition and homeostasis resolved by integrating proteomics and quantitative imaging. *Cytoskeleton (Hoboken)*. 70:741–754. <https://doi.org/10.1002/cm.21142>
- Bouguenina, H., D. Salaun, A. Mangon, L. Muller, E. Baudelet, L. Camoin, T. Tachibana, S. Cianfèrani, S. Audebert, P. Verdier-Pinard, and A. Badache. 2017. EB1-binding-myomalin protein complex promotes centrosomal microtubules functions. *Proc. Natl. Acad. Sci. USA*. 114: E10687–E10696. <https://doi.org/10.1073/pnas.1705682114>
- Brauchle, E., J. Kasper, R. Daum, N. Schierbaum, C. Falch, A. Kirschniak, T.E. Schäffer, and K. Schenke-Layland. 2018. Biomechanical and biomolecular characterization of extracellular matrix structures in human colon carcinomas. *Matrix Biol.* 68–69:180–193. <https://doi.org/10.1016/j.matbio.2018.03.016>
- Buey, R.M., I. Sen, O. Kortt, R. Mohan, D. Gfeller, D. Veprintsev, I. Kretschmar, J. Scheuermann, D. Neri, V. Zoete, et al. 2012. Sequence determinants of a microtubule tip localization signal (MtLS). *J. Biol. Chem.* 287:28227–28242. <https://doi.org/10.1074/jbc.M112.373928>
- Cadart, C., E. Zlotek-Zlotkiewicz, M. Le Berre, M. Piel, and H.K. Matthews. 2014. Exploring the function of cell shape and size during mitosis. *Dev. Cell.* 29:159–169. <https://doi.org/10.1016/j.devcel.2014.04.009>
- Carreno, S., I. Kouranti, E.S. Glusman, M.T. Fuller, A. Echard, and F. Payre. 2008. Moesin and its activating kinase Slik are required for cortical stability and microtubule organization in mitotic cells. *J. Cell Biol.* 180: 739–746. <https://doi.org/10.1083/jcb.200709161>
- Cazaux, S., A. Sadoun, M. Biarnes-Pelicot, M. Martinez, S. Obeid, P. Bongrand, L. Limozin, and P.-H. Puech. 2016. Synchronizing atomic force microscopy force mode and fluorescence microscopy in real time for immune cell stimulation and activation studies. *Ultramicroscopy*. 160: 168–181. <https://doi.org/10.1016/j.ultramic.2015.10.014>
- Chanet, S., R. Sharan, Z. Khan, and A.C. Martin. 2017. Myosin 2-Induced Mitotic Rounding Enables Columnar Epithelial Cells to Interpret Cortical Spindle Positioning Cues. *Curr. Biol.* 27:3350–3358.e3. <https://doi.org/10.1016/j.cub.2017.09.039>
- Chen, A., L. Ulloa Severino, T.C. Panagiotou, T.F. Moraes, D.A. Yuen, B.D. Lavoie, and A. Wilde. 2021. Inhibition of polar actin assembly by astral microtubules is required for cytokinesis. *Nat. Commun.* 12:2409. <https://doi.org/10.1038/s41467-021-22677-0>
- Chugh, P., A.G. Clark, M.B. Smith, D.A.D. Cassani, K. Dierkes, A. Ragab, P.P. Roux, G. Charras, G. Salbreux, and E.K. Paluch. 2017. Actin cortex architecture regulates cell surface tension. *Nat. Cell Biol.* 19:689–697. <https://doi.org/10.1038/ncb3525>
- Clausen, M.P., H. Colin-York, F. Schneider, C. Eggeling, and M. Fritzsche. 2017. Dissecting the actin cortex density and membrane-cortex distance in living cells by super-resolution microscopy. *J. Phys. D Appl. Phys.* 50: 064002. <https://doi.org/10.1088/1361-6463/aa52a1>
- Dao, V.T., A.G. Dupuy, O. Gavet, E. Caron, and J. de Gunzburg. 2009. Dynamic changes in Rap1 activity are required for cell retraction and spreading during mitosis. *J. Cell Sci.* 122:2996–3004. <https://doi.org/10.1242/jcs.041301>
- Daou, P., S. Hasan, D. Breitsprecher, E. Baudelet, L. Camoin, S. Audebert, B.L. Goode, and A. Badache. 2014. Essential and nonredundant roles for Diaphanous formins in cortical microtubule capture and directed cell migration. *Mol. Biol. Cell.* 25:658–668. <https://doi.org/10.1091/mbc.e13-08-0482>
- di Pietro, F., A. Echard, and X. Morin. 2016. Regulation of mitotic spindle orientation: an integrated view. *EMBO Rep.* 17:1106–1130. <https://doi.org/10.15252/embr.201642292>
- Du, Q., P.T. Stukenberg, and I.G. Macara. 2001. A mammalian Partner of inscuteable binds NuMA and regulates mitotic spindle organization. *Nat. Cell Biol.* 3:1069–1075. <https://doi.org/10.1038/ncb1201-1069>
- Ge, W., K. Zhao, X. Wang, H. Li, M. Yu, M. He, X. Xue, Y. Zhu, C. Zhang, Y. Cheng, et al. 2017. iASPP Is an Antioxidative Factor and Drives Cancer Growth and Drug Resistance by Competing with Nrf2 for Keap1 Binding. *Cancer Cell.* 32:561–573.e6. <https://doi.org/10.1016/j.ccell.2017.09.008>
- Hein, M.Y., N.C. Hubner, I. Poser, J. Cox, N. Nagaraj, Y. Toyoda, I.A. Gak, I. Weisswange, J. Mansfeld, F. Buchholz, et al. 2015. A human interactome in three quantitative dimensions organized by stoichiometries and abundances. *Cell.* 163:712–723. <https://doi.org/10.1016/j.cell.2015.09.053>
- Hosseini, K., A. Taubenberger, C. Werner, and E. Fischer-Friedrich. 2020. EMT-Induced Cell-Mechanical Changes Enhance Mitotic Rounding Strength. *Adv. Sci. (Weinh.)*. 7:2001276. <https://doi.org/10.1002/adv.202001276>
- Hotta, A., T. Kawakatsu, T. Nakatani, T. Sato, C. Matsui, T. Sukezane, T. Akagi, T. Hamaji, I. Grigoriev, A. Akhmanova, et al. 2010. Laminin-based cell adhesion anchors microtubule plus ends to the epithelial cell basal cortex through LL5 $\alpha/\beta$ . *J. Cell Biol.* 189:901–917. <https://doi.org/10.1083/jcb.200910095>
- Jiang, L., M.K. Siu, O.G. Wong, K.F. Tam, X. Lu, E.W. Lam, H.Y. Ngan, X.F. Le, E.S. Wong, L.J. Monteiro, et al. 2011. iASPP and chemoresistance in ovarian cancers: effects on paclitaxel-mediated mitotic catastrophe. *Clin. Cancer Res.* 17:6924–6933. <https://doi.org/10.1158/1078-0432.CCR-11-0588>
- Jiang, K., G. Toedt, S. Montenegro Gouveia, N.E. Davey, S. Hua, B. van der Vaart, I. Grigoriev, J. Larsen, L.B. Pedersen, K. Bezstarosti, et al. 2012. A Proteome-wide screen for mammalian SxIP motif-containing microtubule plus-end tracking proteins. *Curr. Biol.* 22:1800–1807. <https://doi.org/10.1016/j.cub.2012.07.047>
- Jontes, J.D., and R.A. Milligan. 1997. Brush border myosin-I structure and ADP-dependent conformational changes revealed by cryoelectron microscopy and image analysis. *J. Cell Biol.* 139:683–693. <https://doi.org/10.1083/jcb.139.3.683>
- Kanaba, T., R. Maesaki, T. Mori, Y. Ito, T. Hakoshima, and M. Mishima. 2013. Microtubule-binding sites of the CH domain of EB1 and its auto-inhibition revealed by NMR. *Biochim. Biophys. Acta.* 1834:499–507. <https://doi.org/10.1016/j.bbapap.2012.10.013>
- Kannan, N., and V.W. Tang. 2018. Myosin-Ic promotes E-cadherin tension and force-dependent recruitment of  $\alpha$ -actinin to the epithelial cell junction. *J. Cell Sci.* 131:jcs.211334. <https://doi.org/10.1242/jcs.211334>
- Kern, D.M., P.K. Nicholls, D.C. Page, and I.M. Cheeseman. 2016. A mitotic SKAP isoform regulates spindle positioning at astral microtubule plus ends. *J. Cell Biol.* 213:315–328. <https://doi.org/10.1083/jcb.201510117>
- Kiyomitsu, T. 2015. Mechanisms of daughter cell-size control during cell division. *Trends Cell Biol.* 25:286–295. <https://doi.org/10.1016/j.tcb.2014.12.003>
- Kunda, P., A.E. Pelling, T. Liu, and B. Baum. 2008. Moesin controls cortical rigidity, cell rounding, and spindle morphogenesis during mitosis. *Curr. Biol.* 18:91–101. <https://doi.org/10.1016/j.cub.2007.12.051>
- Lancaster, O.M., M. Le Berre, A. Dimitracopoulos, D. Bonazzi, E. Zlotek-Zlotkiewicz, R. Picone, T. Duke, M. Piel, and B. Baum. 2013. Mitotic rounding alters cell geometry to ensure efficient bipolar spindle formation. *Dev. Cell.* 25: 270–283. <https://doi.org/10.1016/j.devcel.2013.03.014>
- Leonetti, M.D., S. Sekine, D. Kamiyama, J.S. Weissman, and B. Huang. 2016. A scalable strategy for high-throughput GFP tagging of endogenous human proteins. *Proc. Natl. Acad. Sci. USA.* 113:E3501–E3508. <https://doi.org/10.1073/pnas.1606731113>



- Levental, K.R., H. Yu, L. Kass, J.N. Lakins, M. Egeblad, J.T. Erler, S.F.T. Fong, K. Csiszar, A. Giaccia, W. Weninger, et al. 2009. Matrix crosslinking forces tumor progression by enhancing integrin signaling. *Cell*. 139: 891–906. <https://doi.org/10.1016/j.cell.2009.10.027>
- Liu, Y., N.V. Belkina, C. Park, R. Nambiar, S.M. Loughhead, G. Patino-Lopez, K. Ben-Aissa, J.-J. Hao, M.J. Kruhlik, H. Qi, et al. 2012. Constitutively active ezrin increases membrane tension, slows migration, and impedes endothelial transmigration of lymphocytes in vivo in mice. *Blood*. 119: 445–453. <https://doi.org/10.1182/blood-2011-07-368860>
- Lu, M.S., and C.A. Johnston. 2013. Molecular pathways regulating mitotic spindle orientation in animal cells. *Development*. 140:1843–1856. <https://doi.org/10.1242/dev.087627>
- Lu, M., H. Breysens, V. Salter, S. Zhong, Y. Hu, C. Baer, I. Ratnayaka, A. Sullivan, N.R. Brown, J. Endicott, et al. 2013. Restoring p53 function in human melanoma cells by inhibiting MDM2 and cyclin B1/CDK1-phosphorylated nuclear iASPP. *Cancer Cell*. 23:618–633. <https://doi.org/10.1016/j.ccr.2013.03.013>
- Lu, Q., J. Li, F. Ye, and M. Zhang. 2015. Structure of myosin-1c tail bound to calmodulin provides insights into calcium-mediated conformational coupling. *Nat. Struct. Mol. Biol.* 22:81–88. <https://doi.org/10.1038/nsmb.2923>
- Luxenburg, C., H.A. Pasolli, S.E. Williams, and E. Fuchs. 2011. Developmental roles for Srf, cortical cytoskeleton and cell shape in epidermal spindle orientation. *Nat. Cell Biol.* 13:203–214. <https://doi.org/10.1038/ncb2163>
- Machicoane, M., C.A. de Frutos, J. Fink, M. Rocancourt, Y. Lombardi, S. Garel, M. Piel, and A. Echard. 2014. SLK-dependent activation of ERMs controls LGN-NuMA localization and spindle orientation. *J. Cell Biol.* 205: 791–799. <https://doi.org/10.1083/jcb.201401049>
- Maiato, H., A.M. Gomes, F. Sousa, and M. Barisic. 2017. Mechanisms of Chromosome Congression during Mitosis. *Biology (Basel)*. 6:13. <https://doi.org/10.3390/biology6010013>
- Matthews, H.K., and B. Baum. 2012. The metastatic cancer cell cortex: an adaptation to enhance robust cell division in novel environments? *BioEssays*. 34:1017–1020. <https://doi.org/10.1002/bies.201200109>
- Matthews, H.K., S. Ganguli, K. Plak, A.V. Taubenberger, Z. Win, M. Williamson, M. Piel, J. Guck, and B. Baum. 2020. Oncogenic Signaling Alters Cell Shape and Mechanics to Facilitate Cell Division under Confinement. *Dev. Cell*. 52:563–573.e3. <https://doi.org/10.1016/j.devcel.2020.01.004>
- McIntosh, B.B., and E.M. Ostap. 2016. Myosin-I molecular motors at a glance. *J. Cell Sci.* 129:2689–2695. <https://doi.org/10.1242/jcs.186403>
- Morris, E.V., L. Cerundolo, M. Lu, C. Verrill, F. Fritzsche, M.J. White, G.N. Thalmann, C.S. ten Donkelaar, I. Ratnayaka, V. Salter, et al. 2014. Nuclear iASPP may facilitate prostate cancer progression. *Cell Death Dis.* 5: e1492. <https://doi.org/10.1038/cddis.2014.442>
- Nagelkerke, A., J. Bussink, A.E. Rowan, and P.N. Span. 2015. The mechanical microenvironment in cancer: How physics affects tumours. *Semin. Cancer Biol.* 35:62–70. <https://doi.org/10.1016/j.semcancer.2015.09.001>
- Nakaya, Y., E.W. Sukowati, and G. Sheng. 2013. Epiblast integrity requires CLASP and Dystroglycan-mediated microtubule anchoring to the basal cortex. *J. Cell Biol.* 202:637–651. <https://doi.org/10.1083/jcb.201302075>
- Nambiar, R., R.E. McConnell, and M.J. Tyska. 2009. Control of cell membrane tension by myosin-I. *Proc. Natl. Acad. Sci. USA*. 106:11972–11977. <https://doi.org/10.1073/pnas.0901641106>
- Ramkumar, N., and B. Baum. 2016. Coupling changes in cell shape to chromosome segregation. *Nat. Rev. Mol. Cell Biol.* 17:511–521. <https://doi.org/10.1038/nrm.2016.75>
- Roux, K.J., D.I. Kim, M. Raida, and B. Burke. 2012. A promiscuous biotin ligase fusion protein identifies proximal and interacting proteins in mammalian cells. *J. Cell Biol.* 196:801–810. <https://doi.org/10.1083/jcb.201112098>
- Sadoun, A., and P.-H. Puech. 2017. Quantifying CD95/cl-CD95L Implications in Cell Mechanics and Membrane Tension by Atomic Force Microscopy Based Force Measurements. In *CD95: Methods and Protocols*. P. Legembre, editor. Springer, New York, NY. 139–151. [https://doi.org/10.1007/978-1-4939-6780-3\\_14](https://doi.org/10.1007/978-1-4939-6780-3_14)
- Seetapun, D., B.T. Castle, A.J. McIntyre, P.T. Tran, and D.J. Odde. 2012. Estimating the microtubule GTP cap size in vivo. *Curr. Biol.* 22:1681–1687. <https://doi.org/10.1016/j.cub.2012.06.068>
- Sen, I., D. Veprintsev, A. Akhmanova, and M.O. Steinmetz. 2013. End binding proteins are obligatory dimers. *PLoS One*. 8:e74448. <https://doi.org/10.1371/journal.pone.0074448>
- Serres, M.P., M. Samwer, B.A. Truong Quang, G. Lavoie, U. Perera, D. Görlich, G. Charras, M. Petronczki, P.P. Roux, and E.K. Paluch. 2020. F-Actin Interactome Reveals Vimentin as a Key Regulator of Actin Organization and Cell Mechanics in Mitosis. *Dev. Cell*. 52:210–222.e7. <https://doi.org/10.1016/j.devcel.2019.12.011>
- Shimizu, Y., S.M.A. Haghparast, T. Kihara, and J. Miyake. 2012. Cortical rigidity of round cells in mitotic phase and suspended state. *Micron*. 43: 1246–1251. <https://doi.org/10.1016/j.micron.2012.03.011>
- Skene-Arnold, T.D., H.A. Luu, R.G. Uhrig, V. De Wever, M. Nimick, J. Maynes, A. Fong, M.N. James, L. Trinkle-Mulcahy, G.B. Moorhead, and C.F. Holmes. 2013. Molecular mechanisms underlying the interaction of protein phosphatase-1c with ASPP proteins. *Biochem. J.* 449:649–659. <https://doi.org/10.1042/BJ20120506>
- Stehbens, S.J., M. Paszek, H. Pemble, A. Ettinger, S. Gierke, and T. Wittmann. 2014. CLASPs link focal-adhesion-associated microtubule capture to localized exocytosis and adhesion site turnover. *Nat. Cell Biol.* 16: 558–573. <https://doi.org/10.1038/ncb2975>
- Taubenberger, A.V., B. Baum, and H.K. Matthews. 2020. The Mechanics of Mitotic Cell Rounding. *Front. Cell Dev. Biol.* 8:687. <https://doi.org/10.3389/fcell.2020.00687>
- Toyoda, Y., C.J. Cattin, M.P. Stewart, I. Poser, M. Theis, T.V. Kurzchalia, F. Buchholz, A.A. Hyman, and D.J. Müller. 2017. Genome-scale single-cell mechanical phenotyping reveals disease-related genes involved in mitotic rounding. *Nat. Commun.* 8:1266. <https://doi.org/10.1038/s41467-017-01147-6>
- Venit, T., A. Kalendová, M. Petr, R. Dzijak, L. Pastorek, J. Rohožková, J. Malohlava, and P. Hozák. 2016. Nuclear myosin I regulates cell membrane tension. *Sci. Rep.* 6:30864. <https://doi.org/10.1038/srep30864>
- Zhang, X., M. Wang, C. Zhou, S. Chen, and J. Wang. 2005. The expression of iASPP in acute leukemias. *Leuk. Res.* 29:179–183. <https://doi.org/10.1016/j.leukres.2004.07.001>
- Zhou, Y., R. Millott, H.J. Kim, S. Peng, R.A. Edwards, T. Skene-Arnold, M. Hammel, S.P. Lees-Miller, J.A. Tainer, C.F.B. Holmes, and J.N.M. Glover. 2019. Flexible Tethering of ASPP Proteins Facilitates PP-1c Catalysis. *Structure*. 27:1485–1496.e4. <https://doi.org/10.1016/j.str.2019.07.012>

## Supplemental material

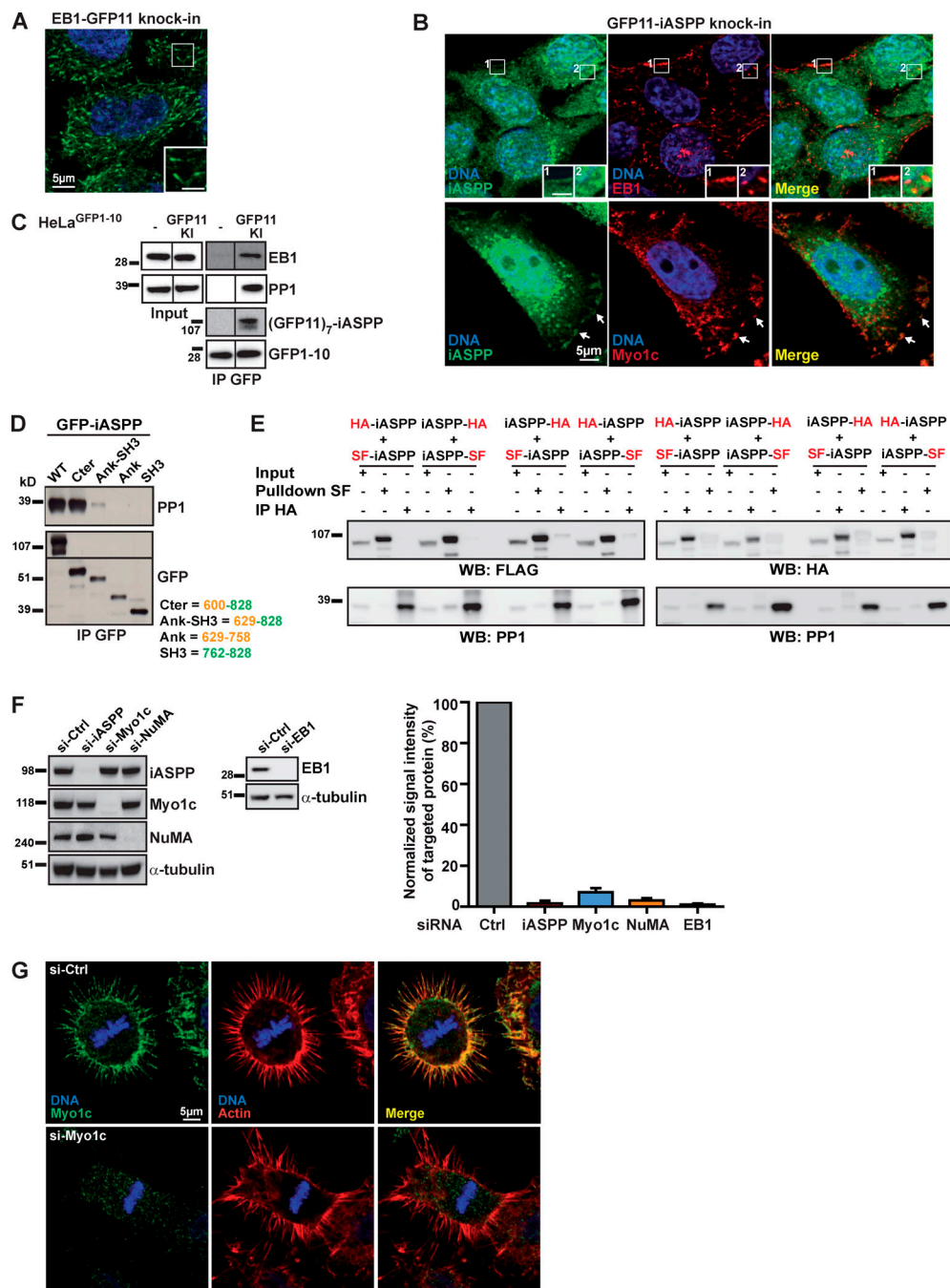


**Figure S1. Validation of EB1-GFP11 and GFP11-iASPP knock-in cells, siRNAs used in the study, and the lack of iASPP homodimerization.** (A) Endogenous EB1, C-terminally tagged with GFP by knock-in (KI) of GFP11 in HeLa<sup>GFP1-10</sup>, localizes to microtubule plus-ends as expected. Insert, zoomed image of the boxed region; scale bar is 10  $\mu$ m. (B) Endogenous iASPP N-terminally tagged with GFP by knock-in of (GFP11)<sub>7</sub> in HeLa<sup>GFP1-10</sup>. iASPP is present in the cytosol, in various types of condensates, and in cortical areas. Co-labeling of EB1 or Myo1c reveals the areas of iASPP and EB1/Myo1c labeling overlap, including cortical areas (arrows and insert 1). Endogenous iASPP partially overlaps with EB1 at plus-ends (insert 2) but does not form comets. Inserts, zoomed images of the boxed regions; scale bar is 10  $\mu$ m. (C) Endogenous iASPP tagged with GFP interacts with endogenous EB1. iASPP was tagged with N-terminal knock-in of (GFP11)<sub>7</sub> in HeLa<sup>GFP1-10</sup> cells. GFP-iASPP was pulled down via GFP-Trap, and EB1 and PP1 coprecipitation was analyzed by WB. (D) Interaction of iASPP with PP1 requires the RARL motif, the Ank repeats, and the SH3 domain. The indicated GFP-tagged iASPP constructs were coexpressed in HEK293 cells before IP with GFP-Trap and WB of the GFP constructs and PP1. Color code corresponds to functional domains as in Fig. 1 E and Fig. 2. (E) iASPP does not homodimerize. The indicated HA-tagged and SF-tagged iASPP constructs were coexpressed in HEK293 cells before IP with HA-conjugated beads or Strep-Tactin Sepharose beads and analyzed by WB. Regardless of the position of the tags, the iASPP constructs do not coprecipitate, in contrast to PP1. Note that 1/10 of the sample was used to verify the efficacy of the IP/pulldown; the rest was used to verify the coprecipitation. (F) Efficiency of iASPP (si-iASPP), Myo1c (si-Myo1c), NuMA (si-NuMA), and EB1 (si-EB1) siRNAs. HeLa cells were transfected with the indicated siRNA before WB analysis with the corresponding antibodies (right) and quantification (left).  $\alpha$ -Tubulin was used as loading control. The bar graph shows the means and SEM of three independent experiments. Signal intensity was normalized to the signal intensity of  $\alpha$ -tubulin, and Ctrl siRNA was set to 100%. (G) Myo1c associates with the actomyosin cortex. Myo1c subcellular localization was verified by IF and phalloidin-based F-actin labeling.



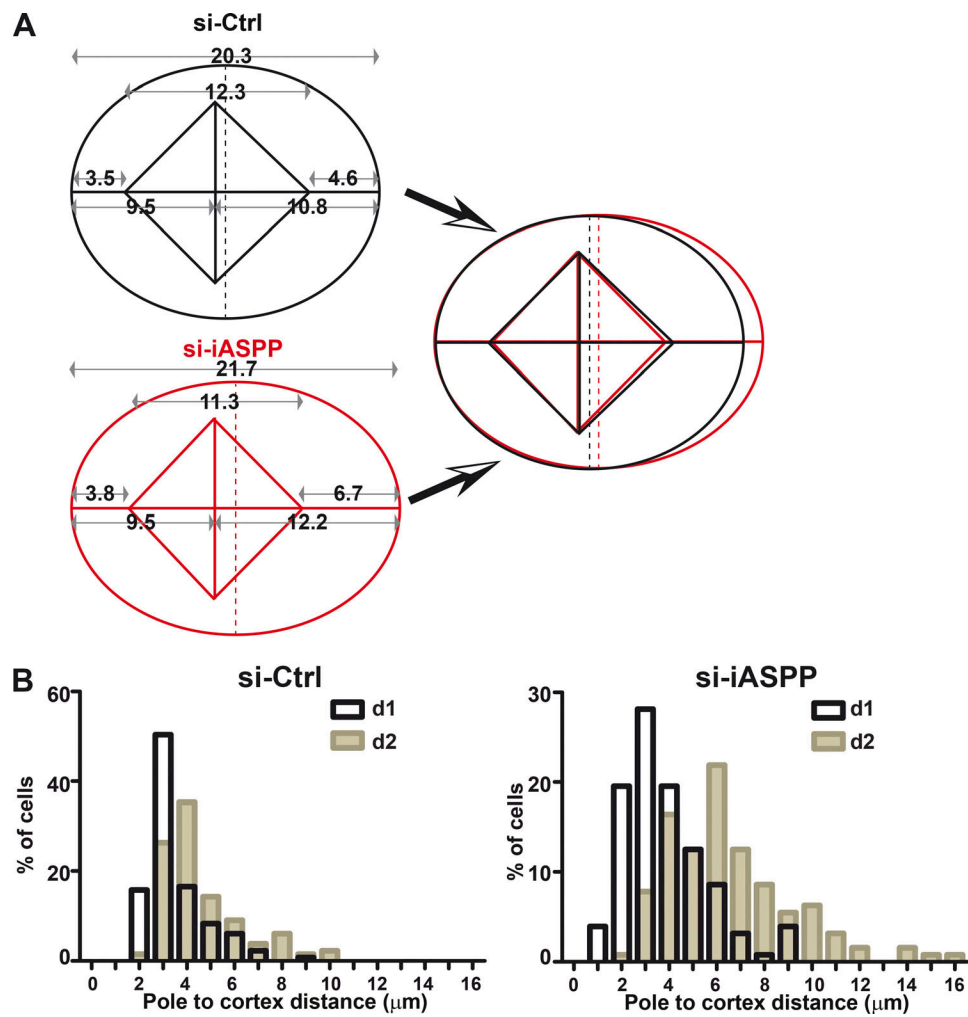


Figure S2. **Impact of iASPP knockdown on mitotic HeLa cells.** (A) Schematic showing the average control HeLa cell and the average iASPP knockdown HeLa cell. HeLa cells were transfected with control (si-Ctrl) or iASPP (si-iASPP) targeting siRNA. Mitotic spindle, centrosomes, and chromosomes of metaphase HeLa cells were visualized by IF and DAPI staining before measuring the cell length (at the level of the centrosomes), spindle size, hemi-spindle size, pole-to-cortex distance, and pole-to-metaphase plate distance. Data were collected from 128 and 133 cells, respectively, obtained in three independent experiments. (B) Histograms of the cell distribution of pole-to-cortex distances in control cells (left) and iASPP knockdown cells (right) showing that iASPP knockdown induced a strong pole-to-cortex asymmetry.

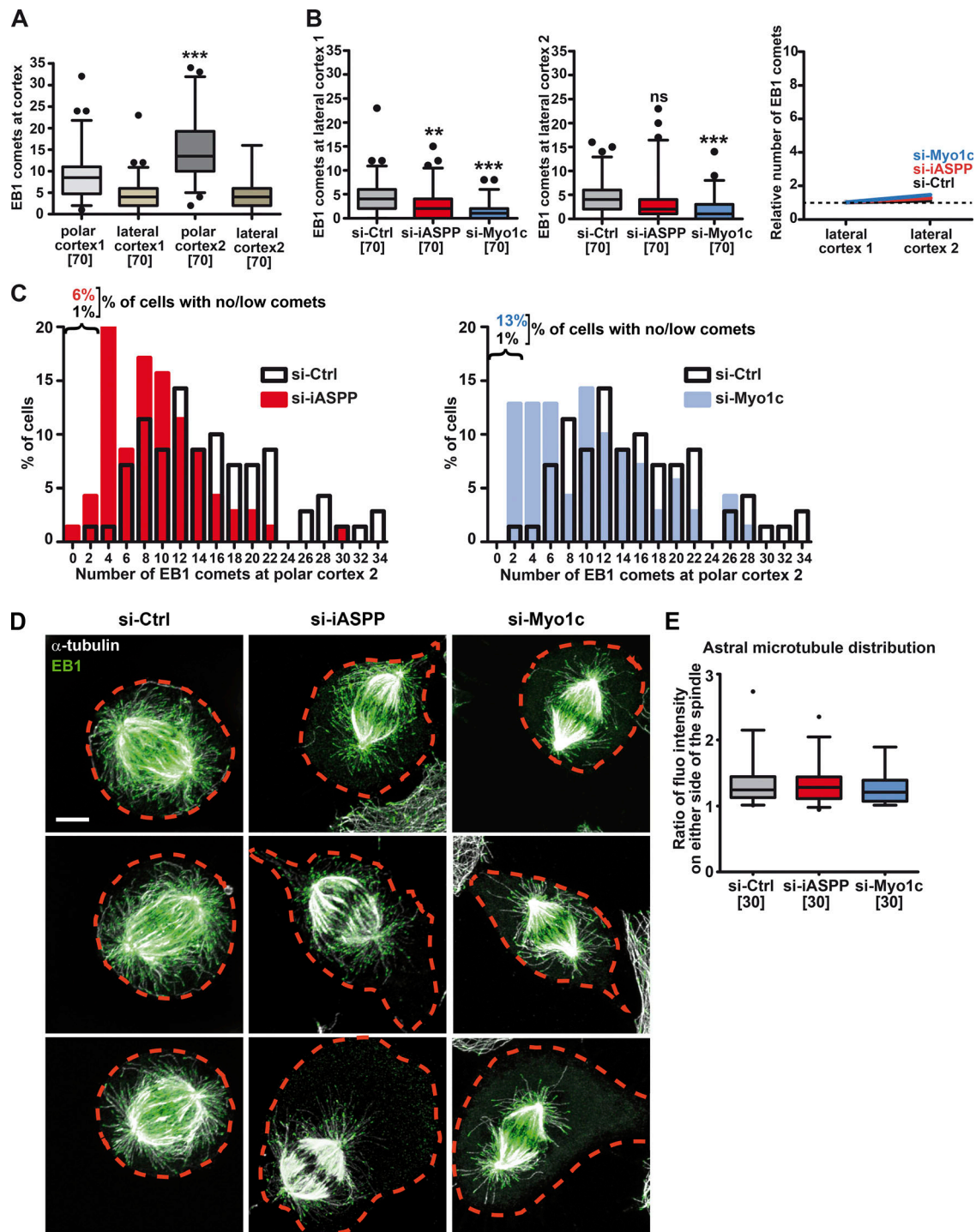
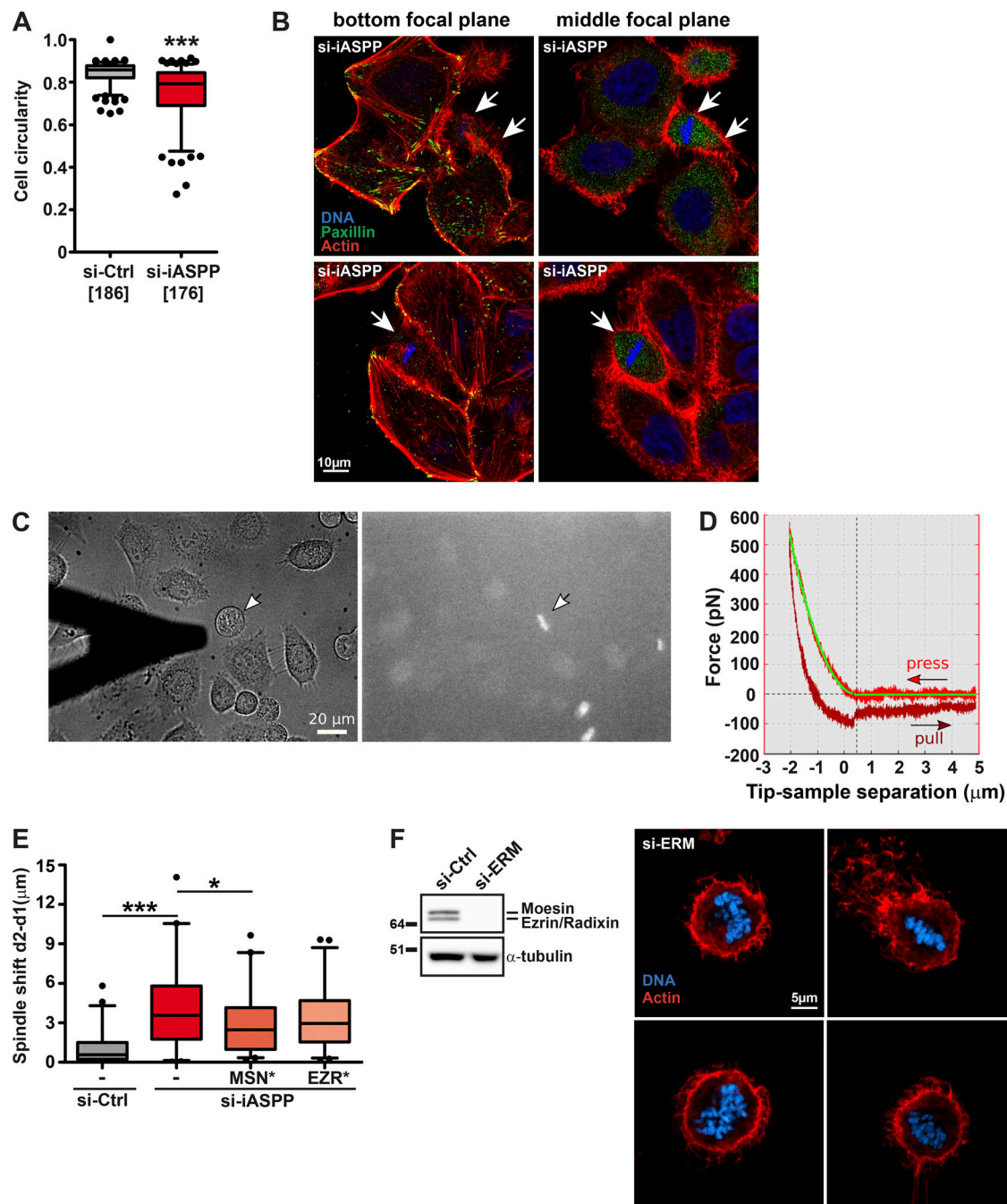


Figure S3. **Impact of iASPP and Myo1c knockdown on astral microtubules.** (A–E) HeLa cells were transfected with control (si-Ctrl), iASPP (si-iASPP), or Myo1c (si-Myo1c) siRNA. Microtubules, microtubule plus-ends, and chromosomes were visualized by confocal microscopy. (A–C) The EB1 comets that reached the polar or lateral cortices (as defined in Fig. 5 B) were counted. (A) The distribution of astral microtubules that reached the polar cortex on either side is slightly asymmetric. (B) The number of astral microtubules that reached the lateral cortices is reduced upon iASPP or Myo1c knockdown but remains symmetrically distributed (right, dashed line is set at 1). (C) Histograms of cell distribution according to cortical comet number at polar cortex 2 illustrate the observation that astral microtubules remained captured on one side of the spindle. (D and E) The density of astral microtubules on either side of the spindle was quantified. (D) Representative maximum image projections are shown. Scale bar is 10  $\mu$ m. (E) In contrast to astral microtubule capture, astral microtubule density remains symmetrically distributed in iASPP and Myo1c knockdown cells. Data were collected from three independent experiments. The number of cells analyzed is indicated between brackets. The unpaired two-tailed t test with Welch correction was used to determine if the difference was significant between data groups. \*\*\*,  $P < 0.001$ ; \*\*,  $P < 0.01$ . fluo, fluorescence.



**Figure S4. Impact of iASPP knockdown on cell circularity and focal adhesions; impact of ERM proteins on mitotic cell morphology; AFM methodology.** (A) iASPP silencing prevents rounding of mitotic cells. HeLa cells were transfected with control (si-Ctrl) or iASPP (si-iASPP) siRNA. Microtubules and chromosomes were visualized by IF, z-stacks were collected, and cell circularity was calculated from maximum-intensity projection images. The number of cells analyzed is indicated between brackets. (B) Mitotic iASPP knockdown cells disassemble stress fibers and focal adhesions. Adhesions, actin filaments, and chromosomes were labeled with anti-paxillin antibody, TRITC-phalloidin, and DAPI staining, respectively. Representative images are shown. Two focal planes are presented to visualize focal adhesions (bottom focal plane) and the metaphase plate (middle focal plane). Arrows indicate mitotic cells. Note the absence of focal adhesions and stress fibers in metaphase cells compared with neighboring interphase cells. (C and D) Using AFM force curves to investigate mitotic cell mechanics. (C) Top view phase contrast (left) and mCherry-H2B fluorescence (right) micrographs showing a cantilever tip positioned near a mitotic cell. Note the typical mitotic cell morphology and chromosome alignment (arrow). (D) Typical pressing and pulling force curves. Elastic measurements (Young modulus) were extracted from a fit using a Hertz-like model (green curve) on the pressing curve over the greyed region. Note that the adhesion as observed on the retract curve was relatively weak so that using Hertz model was reasonable. (E) Expression of active moesin or ezrin partly restores mitotic spindle centering. HeLa cells were transfected with control or iASPP siRNA together with GFP, GFP-tagged moesin T558D (MSN\*), or GFP-tagged ezrin T567D (EZR\*) before cell labeling and evaluation of mitotic spindle positioning as in Fig. 3. (F) ERMs do not contribute to HeLa cell mitotic rounding. HeLa cells were transfected with siRNA targeting all three ERMs before analysis by WB (left) and confocal microscopy (right); actin filaments and chromosomes were labeled with TRITC-phalloidin and DAPI staining, respectively. Representative cells are shown. Scale bar is 5  $\mu$ m. Data are collected from three independent experiments. The unpaired two-tailed *t* test with Welch correction was used to determine if the difference was significant between data groups. \*\*\*,  $P < 0.001$ ; \*,  $P < 0.05$ .



